

---

# ADAPTIVE DIFFUSION POSTERIOR SAMPLING FOR DATA AND MODEL FUSION OF COMPLEX NONLINEAR DYNAMICAL SYSTEMS

---

**Dibyajyoti Chakraborty**

College of Information Sciences and Technology,  
Pennsylvania State University,  
University Park, 16802, PA, USA

**Hojin Kim, Romit Maulik**

School of Mechanical Engineering,  
Purdue University,  
West Lafayette, 47907, IN, USA

## ABSTRACT

High-fidelity numerical simulations of chaotic, high dimensional nonlinear dynamical systems are computationally expensive, necessitating the development of efficient surrogate models. Most surrogate models for such systems are deterministic, for example when neural operators are involved. However, deterministic models often fail to capture the intrinsic distributional uncertainty of chaotic systems. This work presents a surrogate modeling formulation that leverages generative machine learning, where a deep learning diffusion model is used to probabilistically forecast turbulent flows over long horizons. We introduce a multi-step autoregressive diffusion objective that significantly enhances long-rollout stability compared to standard single-step training. To handle complex, unstructured geometries, we utilize a multi-scale graph transformer architecture incorporating diffusion preconditioning and voxel-grid pooling. More importantly, our modeling framework provides a unified platform that also predicts spatiotemporally important locations for sensor placement, either via uncertainty estimates or through an error-estimation module. Finally, the observations of the ground truth state at these dynamically varying sensor locations are assimilated using diffusion posterior sampling requiring no retraining of the surrogate model. We present our methodology on two-dimensional homogeneous and isotropic turbulence and for a flow over a backwards-facing step, demonstrating its utility in forecasting, adaptive sensor placement, and data assimilation for high dimensional chaotic systems.

## 1 Introduction

High-fidelity simulation of chaotic dynamical systems such as turbulent flows remains prohibitively expensive at practically relevant Reynolds numbers, with DNS requiring  $\mathcal{O}(Re^{9/4})$  degrees of freedom in three dimensions [1]. While deep learning surrogates have dramatically reduced this cost, deterministic models share a fundamental statistical deficiency: they collapse the full conditional distribution of the true stochastic system to a point prediction. For any chaotic system with intrinsic state variance, this incurs an irreducible per-step Wasserstein error that accumulates exponentially over the forecast horizon. Diffusion models [2, 3] resolve this by learning the full conditional distribution, making their per-step mismatch entirely reducible by training (Ref. Section 3.1 for further details). In several practical applications, training data from the dynamical system that may be used by a surrogate, is available on point clouds or meshes that result from numerical discretizations of governing laws. This brings forth the need to design accurate diffusion-based surrogate models that are specialized for forecasting high dimensional chaotic dynamical systems on unstructured meshes.

Beyond forecasting, practical deployment requires fusing model predictions with sparse runtime observations from physical sensors. Diffusion posterior sampling [4, 5] achieves this by augmenting each denoising step with a likelihood

gradient, steering the generative process toward the posterior without retraining. This raises a natural follow-on question: *where* should sensors be placed to maximally reduce posterior uncertainty? In the context of Bayesian data assimilation, there exist several techniques for optimal sensor placement that are both physics and data-driven [6, 7, 8]. Several approaches rely on information theoretic approaches such as A/D/E optimal design which are optimization-based strategies that rely on assumptions for the shape of the posterior distribution [9]. Observability-based approaches based on control theory choose (typically fixed) sensor locations to maximize a metric of the observability Gramian [10, 11]. When forecasting with projection-based reduced-order models, QR pivoting is a common approach that leverages the identified proper orthogonal decomposition modes from training data [7]. Discrete empirical interpolation methods also identify sensor placement strategies that identify points which are important for nonlinear term reconstruction [12]. However, most approaches for sensor placement tend to be fixed or require expensive online computations which reduces their utility for real-time data and model fusion. To address this gap, we propose two approaches for optimal sensor placement using a trained diffusion model. The first approach relies on the fact that a diffusion model can be sampled to generate ensembles of forecasts. A diffusion ensemble is itself a spatially-resolved uncertainty field, making it a direct and principled guide for sensor placement - closing the loop between inference and observation in a unified active inference framework. However, uncertainty guided sensor placement suffers from increased computational costs for ensemble generation via sampling the diffusion model. To complement this, we propose a metamodeling strategy that uses *another* model to predict the rollout error of the surrogate and to use spatial concentrations of this predicted error to sample new points efficiently.

Based on these, our work delivers four contributions : **(i)** A multi-step autoregressive diffusion training objective over a  $K$ -step rollout that significantly improves long-horizon stability over single-step training. **(ii)** A multi-scale Graph Transformer diffusion architecture combining EDM preconditioning [3], AdaLN-Zero conditioning [13], and hierarchical voxel-grid pooling to forecast in unstructured meshes. **(iii)** Two adaptive sensor placement strategies: a learned predictive error network based estimator and a diffusion ensemble-variance-based estimator targeting observations where the generative prior has most uncertainty. **(iv)** A topology-aware greedy selection algorithm with spatial suppression that enforces minimum sensor separation, preventing redundant clustering in localized high-uncertainty regions. We validate the framework on two-dimensional forced homogeneous isotropic turbulence at  $Re = 1000$  and flow over a backwards-facing step at  $Re = 26,000$  on an unstructured high-dimensional finite-element mesh. The associated codes are available at [https://github.com/ISCLPurdue/chaos\\_gen](https://github.com/ISCLPurdue/chaos_gen).

## 1.1 Related Works

Surrogate modeling replaces expensive high-fidelity simulations with computationally efficient approximation that reproduce the input-output behavior of a target system. Classical methods such as Gaussian processes[14], radial basis functions [15], and polynomial response surfaces [16, 17] provide well-calibrated uncertainty estimates for low-dimensional systems, but their scalability rapidly degrades with the dimensionality of the problem [18]. Deep neural operator architectures have substantially extended the scope of tractable surrogate tasks: the Fourier Neural Operator [19] learns resolution-invariant solution operators for parametric PDEs, while DeepONet [20] exploits the universal approximation theorem for operators to generalize across functional inputs. For time-dependent systems, recurrent architectures such as LSTM [21] and gated recurrent units [22] capture long-range temporal dependencies and have been applied to data-driven forecasting of high-dimensional chaotic attractors [23, 24]. Specialized surrogate models[25, 26, 27, 28] have further demonstrated competitive performance in reduced-order modeling of chaotic systems such as turbulent flows. Despite these advances, deterministic surrogates produce only point predictions and cannot represent the distributional uncertainty intrinsic to stochastic or chaotic dynamics. Diffusion models [29, 2, 30, 3] resolve this limitation by learning a reverse-time stochastic differential equation that maps Gaussian noise to complex high-dimensional distributions. Their superior mode coverage over GANs [31] and natural extension to video and spatiotemporal sequences [32] make them especially attractive for dynamical system surrogates. Some diffusion-inspired surrogate models, such as PDE-Refiner [33], further demonstrate that an iterative refinement process improves long-rollout and spectral accuracy relative to one-step neural solvers. Moreover, experiments in previous work have shown the advantages of applying generative diffusion models over traditional ML surrogate models for a variety of high dimensional dynamical systems [34, 35, 36, 37, 38, 39, 40, 41, 42, 43]. In this work, we perform a theoretical comparison of long term error propagation for deterministic and generative surrogate models.

Unstructured meshes and irregular topologies that arise naturally in computational fluid dynamics and structural mechanics have been tackled by Graph neural networks (GNNs) based surrogate models. Sanchez-Gonzalez et al. [44] established a foundational encoder-processor-decoder GNN capable of simulating complex multi-physics on particle and mesh representations. Pfaff et al. [45] specialized this architecture to finite-element meshes, demonstrating orders-of-magnitude speed-up over high-fidelity solvers. Message-passing neural PDE solvers [46] and multi-scale GNN variants [47] further improve accuracy on flows with different spatial scales. Another direction of work shows that the combination of differentiable PDE solvers with GNN surrogates [48, 49] yields physically consistent predictions

on complex problems. Furthermore, GraphCast [50] uses a hierarchical graph transformer to achieve state-of-the-art global weather prediction, underscoring the scalability of graph-based surrogates. However, as in the previous case, deterministic GNN surrogates produce only point predictions and cannot capture the distributional spread of stochastic or turbulent states. Graph diffusion models have been shown to be successful in several specific tasks such as molecule synthesis [51, 52, 53], protein folding [54], weather forecasting [55], and traffic and air quality prediction [56]. Sparse polynomial surrogates for diffusion processes on graphs [57] provide convergence guarantees for least squares and compressed sensing recovery. Most directly relevant to this work, Lino et al. [58] proposed the Diffusion Graph Network (DGN), a latent diffusion model with a multi-scale GNN processor that samples equilibrium flow field distributions on unstructured meshes, and its SE(3)-equivariant predecessor [59] demonstrated that incorporating geometric symmetry into the score network significantly improves sample fidelity.

Probabilistic surrogates naturally interface with data-assimilation pipelines [60, 61, 62], motivating the posterior-sampling perspective adopted here. Within this framework, the question of *where* to observe is formalized by optimal experimental design (OED), which optimizes sensor placement with respect to information gain [9, 63]. For high-dimensional PDE systems, tractable placement strategies have been developed through sparse selection on POD bases, connecting compressed sensing to structured sensor placement [7]. Active learning extends this idea sequentially: as the surrogate improves, placement is iteratively refined by targeting regions of high posterior uncertainty [64, 65], directly motivating the adaptive strategy used here. Crucially, decoupling sensor placement from inference is suboptimal; co-optimizing sensor layouts with the inference procedure yields substantially tighter posteriors across a range of inverse problems [66, 67]. Separately, diffusion posterior sampling [4, 5] has emerged as a powerful reconstruction framework conditioning the reverse diffusion process on sparse observations. This paradigm has shown promise in sparse reconstruction and model-data fusion [68, 69, 70, 71]. Recent physics-informed diffusion models further embed PDE residuals as constraints during training [72] or sampling [73, 74], enabling data-efficient learning of physical systems and directly underpinning the adaptive diffusion posterior sampling approach proposed in this work. Furthermore, rather than treating sensor placement as a pre-processing step, a diffusion model enables uncertainty from the generative model to *inform* placement, integrating the two into a unified inference loop, as shown further in this work.

Some recent work has explored adaptive sensor placement for physical systems using generative and learning-based methods. Zhao et al. [75] and Son and Lee [76] leverage graph diffusion policies and diffusion-attention mechanisms for adaptive combinatorial sensor placement in power systems and distributed parameter systems, respectively. Vishwasrao et al. [77] introduced Diff-SPORT, combining diffusion posterior sampling with Shapley-value attribution to rank and select sensor locations for urban turbulent flow reconstruction, although modeling temporal dynamics and out-of-distribution generalization remain open. Ma et al. [8] proposed PhySense, coupling a flow-based generative model with projected gradient descent to co-optimize reconstruction and sensor placement with theoretical guarantees. Wang et al. [78] trained a Transformer policy through actor-critic reinforcement learning to iteratively reallocate climate sensors, though without a generative prior for posterior-based field reconstruction. The costs of such added optimization and applications to high dimensional dynamical systems remain unexplored. In contrast, our work unifies autoregressive probabilistic forecasting, diffusion posterior sampling, and a topology-aware adaptive sensor placement in a single closed-loop during inference for high dimensional chaotic systems on unstructured meshes.

## 2 Methods

### 2.1 Diffusion-based Generative Modeling

Diffusion models function as generative priors by reversing a forward stochastic process that gradually degrades data structure until it resembles pure noise. We adopt the Elucidating Diffusion Model (EDM) framework [3], which uses a "variance exploding" forward process. For a clean data sample  $\mathbf{x}_0$  and a noise level  $\sigma \in [\sigma_{\min}, \sigma_{\max}]$ , the noising process is defined as:

$$\mathbf{x}(\sigma) = \mathbf{x}_0 + \sigma \mathbf{n}, \quad \text{where } \mathbf{n} \sim \mathcal{N}(\mathbf{0}, \mathbf{I}). \quad (1)$$

During training, instead of directly predicting added noise, a preconditioned [3] neural network  $F_\theta$  is trained to output the denoised data estimate  $D_\theta(\mathbf{x}(\sigma); \sigma) \approx \mathbf{x}_0$  using a weighted mean squared error over the noise schedule:

$$L(\theta) = \mathbb{E}_{\mathbf{x}_0, \mathbf{n}, \sigma} [\lambda(\sigma) \|\mathbf{x}_0 - D_\theta(\mathbf{x}(\sigma); \sigma)\|^2], \quad (2)$$

where the weighting function  $\lambda(\sigma)$  ensures balance between different levels of noise.

Once trained,  $D_\theta$  is proportional to the score of the data distribution,  $\nabla_{\mathbf{x}} \log p(\mathbf{x}(\sigma))$ , effectively pointing towards the data manifold. This allows for deterministic sampling via the Probability Flow ODE [30, 3]:

$$d\mathbf{x} = \frac{D_\theta(\mathbf{x}(\sigma); \sigma) - \mathbf{x}(\sigma)}{\sigma} d\sigma. \quad (3)$$

Generation is performed by initializing  $\mathbf{x}(\sigma_{\max}) \sim \mathcal{N}(\mathbf{0}, \sigma_{\max}^2 \mathbf{I})$  at a large noise level ( $\sigma_{\max}$ ) and integrating this ODE backward to  $\sigma = 0$ .

## 2.2 Single and Multi-step Training

**Single-Step Denoising Loss.** Following the EDM framework, noise levels are sampled per graph from a log-normal distribution,  $\ln \sigma \sim \mathcal{N}(P_\mu, P_\sigma^2)$ , and the training objective minimizes a noise-weighted mean squared error over node features:

$$\mathcal{L} = \mathbb{E}_{\sigma, \mathbf{n} \sim \mathcal{N}(\mathbf{0}, \sigma^2 \mathbf{I})} \left[ \lambda(\sigma) \|D_\theta(\mathbf{x} + \mathbf{n}; \sigma) - \mathbf{x}\|_F^2 \right], \quad (4)$$

where  $\lambda(\sigma) = (\sigma^2 + \sigma_{data}^2) / (\sigma \sigma_{data})^2$  is the EDM loss weighting that up-weights low-noise predictions,  $\mathbf{n}$  is node-wise Gaussian noise broadcast from the per-graph  $\sigma$ , and  $\|\cdot\|_F$  denotes the Frobenius norm over all nodes and features.

**Multi-Step Autoregressive Loss.** For stable and accurate forecasting over a horizon of  $K$  timesteps, we train the model for multiple timesteps. Given an initial conditioning state  $\mathbf{x}^{(0)}$  (e.g., the current observed field), the model predicts the expected value of the next state, which is then fed back as conditioning for the subsequent step. Concretely, we define the one-step prediction as

$$\hat{\mathbf{x}}^{(k)} = D_\theta(\mathbf{x}^{(k)} + \mathbf{n}^{(k)}; \sigma^{(k)}, \hat{\mathbf{x}}^{(k-1)}), \quad (5)$$

where  $\mathbf{x}^{(k)}$  is the ground-truth target at rollout step  $k$ ,  $\mathbf{n}^{(k)} \sim \mathcal{N}(\mathbf{0}, (\sigma^{(k)})^2 \mathbf{I})$ , and  $\hat{\mathbf{x}}^{(k-1)}$  is the denoised prediction from the previous step used as the conditioning input (with  $\hat{\mathbf{x}}^{(0)} = \mathbf{x}^{(0)}$ ). The multi-step diffusion loss takes a weighted average (with weights  $w(k)$ ) of the single-step EDM objective across the rollout:

$$\mathcal{L}_K = \frac{1}{K} \sum_{k=1}^K w(k) \mathbb{E}_{\sigma^{(k)}, \mathbf{n}^{(k)}} \left[ \lambda(\sigma^{(k)}) \|\hat{\mathbf{x}}^{(k)} - \mathbf{x}^{(k)}\|_F^2 \right]. \quad (6)$$

Gradients are propagated through each step independently; the conditioning  $\hat{\mathbf{x}}^{(k-1)}$  is detached from the computational graph between steps for making the model robust to error growth [46] and prevent gradient explosion over long rollouts [79].

## 2.3 Conditional Generation

To perform conditional generation given sparse or noisy measurements  $\mathbf{y}$ , we aim to sample from the posterior distribution  $p(\mathbf{x}|\mathbf{y})$ . For fixed conditions, for example the previous history of states in a forecasting problem, they can be directly inputted to the network  $D_\theta$  like Equation 5. However, for test time conditions like sparse observations, we employ a posterior sampling strategy. By applying Bayes' rule to the score function, posterior score can be divided into a prior term and a likelihood guidance term:

$$\nabla_{\mathbf{x}(\sigma)} \log p(\mathbf{x}(\sigma)|\mathbf{y}) = \underbrace{\nabla_{\mathbf{x}(\sigma)} \log p(\mathbf{x}(\sigma))}_{\text{Prior (Model)}} + \underbrace{\nabla_{\mathbf{x}(\sigma)} \log p(\mathbf{y}|\mathbf{x}(\sigma))}_{\text{Likelihood (Guidance)}}. \quad (7)$$

Directly computing the likelihood  $p(\mathbf{y}|\mathbf{x}(\sigma))$  is intractable because  $\mathbf{x}(\sigma)$  is a noisy latent variable. Methods such as Diffusion Posterior Sampling (DPS) [4] approximate this term by estimating the clean data  $\hat{\mathbf{x}}_0$  using Tweedie's formula, which is equivalent to the denoiser output:  $\hat{\mathbf{x}}_0 \approx D_\theta(\mathbf{x}(\sigma); \sigma)$  in our case.

We adopt the Score-based Data Assimilation (SDA) approach [5], which improves upon standard DPS by normalizing the gradients with a time-dependent variance estimate. This accounts for the diminishing information content of the measurements at high noise levels. The approximate likelihood gradient used to guide the solver is:

$$\nabla_{\mathbf{x}(\sigma)} \log p(\mathbf{y}|\mathbf{x}(\sigma)) \approx -\nabla_{\mathbf{x}(\sigma)} \frac{\|\mathbf{y} - M(D_\theta(\mathbf{x}(\sigma); \sigma))\|^2}{2(\Sigma_y + \sigma^2 \hat{\Gamma})}, \quad (8)$$

where  $M$  is the measurement operator,  $\Sigma_y$  is the measurement noise variance, and  $\hat{\Gamma}$  is a scalar approximating the Jacobian-prior variance. We employ the Stochastic Posterior Sampler proposed by Chakraborty et al. [70] to solve the reverse process.

## 2.4 Graph Diffusion Architecture

We define a hierarchical graph network  $F_\theta(\mathbf{x}(\sigma); \sigma)$ , where the noisy state  $\mathbf{x}(\sigma)$  consists of node features  $\mathbf{X} \in \mathbb{R}^{N \times F}$ . The architecture follows a U-Net design with symmetric encoder and decoder paths connected by skip connections, using a Graph Transformer backbone conditioned on the noise level  $\sigma$ .

**Input Embedding and Noise Conditioning.** Continuous node positions are lifted to a higher-dimensional representation via Gaussian Fourier projections,

$$\mathbf{h}_{\text{pos}} = [\sin(2\pi\mathbf{W}\mathbf{p}) \parallel \cos(2\pi\mathbf{W}\mathbf{p})], \quad (9)$$

where  $\mathbf{W} \sim \mathcal{N}(0, s^2)$  is a fixed random matrix and  $\mathbf{p} \in \mathbb{R}^d$  is a node position. The concatenation  $[\mathbf{X} \parallel \mathbf{h}_{\text{pos}}]$  is projected to the hidden dimension  $C$  by a linear layer. Edge attributes are constructed from relative positions and Euclidean distances between connected nodes and projected to  $\mathbb{R}^C$ .

The noise level  $\sigma$  is encoded via a sinusoidal embedding followed by an MLP to produce a conditioning vector  $\mathbf{e}_\sigma \in \mathbb{R}^{d_t}$ . This is injected into each block via Adaptive Layer Normalization with zero initialization (AdaLN-Zero):

$$\text{AdaLN}(\mathbf{h}, \mathbf{e}_\sigma) = (1 + \mathbf{y}_s(\mathbf{e}_\sigma)) \odot \text{LayerNorm}(\mathbf{h}) + \mathbf{y}_b(\mathbf{e}_\sigma), \quad (10)$$

where  $\mathbf{y}_s$  and  $\mathbf{y}_b$  are linear projections initialized to zero. The  $(1 + \mathbf{y}_s)$  formulation ensures each block acts as an identity at the start of training.

**Graph Transformer Block.** Between encoder and decoder, two Graph Transformer blocks are applied at the coarsest resolution to allow global information exchange before upsampling begins. Each block applies AdaLN-conditioned Graph Transformer convolution followed by a position-wise feed-forward network (FFN), both with residual connections:

$$\mathbf{h}_i^{(l+1)} = \mathbf{h}_i^{(l)} + \sum_{j \in \mathcal{N}(i)} \alpha_{ij} \mathbf{W}_v \mathbf{h}_j^{(l)}, \quad (11)$$

where the attention weights  $\alpha_{ij}$  are computed from node and edge features. The FFN is applied after a second AdaLN modulation step, also with a residual.

**Hierarchical Pooling and Unpooling.** To capture multi-scale geometric structure, the encoder progressively coarsens the graph through voxel grid pooling, and the decoder restores resolution via distance-weighted interpolation.

*Voxel grid pooling (downsampling).* At each encoder level  $\ell$  with voxel resolution  $r_\ell$ , nodes are assigned to spatial voxels and aggregated by mean pooling within each cluster  $\mathcal{C}$ :

$$\mathbf{p}_{\text{coarse}} = \frac{1}{|\mathcal{C}|} \sum_{j \in \mathcal{C}} \mathbf{p}_j, \quad \mathbf{h}_{\text{coarse}} = \frac{1}{|\mathcal{C}|} \sum_{j \in \mathcal{C}} \mathbf{h}_j. \quad (12)$$

Edges on the coarsened graph are rebuilt by connecting all node pairs within a radius of  $r_\ell \sqrt{2} \cdot 1.5$ .

*KNN interpolation (upsampling).* Features are propagated from coarse to fine resolution using inverse-distance weighting over the  $k$  nearest coarse neighbors  $\mathcal{N}_k(\mathbf{p}_f)$  of each fine node:

$$\mathbf{h}_f = \sum_{c \in \mathcal{N}_k(\mathbf{p}_f)} \frac{w_c}{\sum_m w_m} \mathbf{h}_c, \quad w_c = \|\mathbf{p}_f - \mathbf{p}_c\|_2^{-1}. \quad (13)$$

The interpolated features are concatenated with the corresponding encoder skip features and fused by a linear projection before the subsequent Graph Transformer block.

**Output and Preconditioning.** A global long-skip connection adds the projected input to the final decoder output, preserving low-frequency content. The result is passed through Layer Normalization and a linear output projection to produce the denoised node features  $\hat{\mathbf{x}}$ . The raw network output  $F_\theta$  is then wrapped with noise-level-dependent scaling using an EDM preconditioner[3]:

$$D_\theta(\mathbf{x}; \sigma) = c_{\text{skip}}(\sigma) \mathbf{x} + c_{\text{out}}(\sigma) F_\theta(c_{\text{in}}(\sigma) \mathbf{x}; c_{\text{noise}}(\sigma)), \quad (14)$$

where  $c_{\text{skip}} = \sigma_d^2 / (\sigma^2 + \sigma_d^2)$ ,  $c_{\text{out}} = \sigma \sigma_d / \sqrt{\sigma^2 + \sigma_d^2}$ ,  $c_{\text{in}} = 1 / \sqrt{\sigma^2 + \sigma_d^2}$ , and  $c_{\text{noise}} = \frac{1}{4} \ln \sigma$ , with  $\sigma_d$  denoting the data standard deviation; this rescales inputs and outputs so the network operates in a unit-variance regime across all noise levels. This preconditioning helps to mitigate some of the limitations of a variance exploding diffusion model.

## 2.5 Sensor Placement

Optimal sensor placement is critical for maximizing information gain during data assimilation. To condition the posterior diffusion generation on measurements, we implement three distinct sensor placement strategies. Each strategy selects a fixed budget of  $s$  sensors. All strategies include locations that reside strictly within the spatial boundaries of the domain.

**Random Placement** Under the random sensor placement strategy, sensor locations are sampled uniformly at random from the pool of eligible interior points. This serves as a baseline for comparing other sensor placement strategies.

**Predictive Model-based Placement** We utilize a learned, adaptive strategy that positions sensors in spatial "hot spots" where the pre-trained diffusion model  $D_\theta$  exhibits the highest reconstruction error from the prior, meaning it is least capable of generating the correct values without observation.

To quantify this, we define a ground-truth error field,  $\mathcal{E}_{gt}$ , as the difference between the ground truth and the expected value of the diffusion forecast. This is defined at each node. Since in our diffusion framework, the network directly predicts the expected forecast when denoising a pure noise sample ( $\mathbf{x}(\sigma_{\max}) = \mathbf{x}_0 + \sigma_{\max} \mathbf{n}$ ), this spatial error map is computed as:

$$\mathcal{E}_{gt} = \frac{1}{C} \|\mathbf{x}_0 - D_\theta(\mathbf{x}(\sigma_{\max}); \sigma_{\max})\|_2^2 \quad (15)$$

where the norm is computed over the channel dim only. Since  $\mathbf{x}_0$  is unknown at inference time, we train a secondary predictor network,  $P_\phi$ , to estimate this error field based on available conditioning or previous states  $\mathbf{x}_{\text{cond}}$ . The predictor  $P_\phi$  shares the base architecture of the generative model excluding the noise level conditioning, and minimizes the Huber loss  $\mathcal{H}$  against the ground truth error:

$$\mathcal{L}(\phi) = \mathcal{H}(P_\phi(\mathbf{x}_{\text{cond}}) - \mathcal{E}_{gt}). \quad (16)$$

During inference, the predicted error map  $\hat{\mathcal{E}} = P_\phi(\mathbf{x}_{\text{cond}})$  guides the observation points  $\mathbf{S}$  construction via a topology-aware greedy strategy:

1. **Initialization:** Define the set of candidate spatial locations, excluding domain boundaries.
2. **Greedy Selection:** Iteratively select the location  $i^*$  with the highest predicted error:  $i^* = \text{argmax}_i(\hat{\mathcal{E}}_i)$ .
3. **Topology-aware Suppression:** To ensure broad spatial coverage and prevent sensor clustering, suppress the error values of all candidate locations within a defined local neighborhood (e.g., a spatial radius or structural adjacency distance) of  $i^*$ .
4. **Iteration:** Repeat steps 2 and 3 until the measurement budget is exhausted.

**Uncertainty-Driven Placement** Rather than relying on a parameterized error network, the uncertainty-driven strategy leverages the inherent variance of an active diffusion ensemble. At each sampling step, we compute predictions across  $E$  parallel ensemble members. Let  $\mathbf{x}^{(e)}$  represent the predicted state of the  $e$ -th ensemble member. We calculate the local predictive uncertainty  $u_i$  as the mean standard deviation across the  $C$  feature channels:

$$u_i = \frac{1}{C} \sum_{c=1}^C \text{Std} \left( \{x_{i,c}^{(1)}, x_{i,c}^{(2)}, \dots, x_{i,c}^{(E)}\} \right) \quad (17)$$

Sensors are then placed at the locations exhibiting the highest uncertainty  $u_i$ , using the identical greedy selection algorithm and spatial suppression applied in the predictive method. Although this method does not have any initial cost like training the error model, it requires an ensemble to be generated at every step to estimate the sensor locations.

### 3 Error Analysis

#### 3.1 Autoregressive Surrogates for Stochastic Dynamical Systems

We show that the rate of error propagation in a surrogate model depends on the per-step error, which is non-reducible for a deterministic surrogate, and an exponential growth part which depends on the surrogate's underlying smoothness.

**Setup.** An interesting property of chaotic systems is that although having a deterministic character, they are often treated as a stochastic system due to their extreme sensitivity to initial conditions [80]. Note also, that stochasticity may also arise from unresolved physics, partial observability and model-form uncertainty. The observed or measured states may then be treated as samples from an evolving probability density function [81, 82]. Let the true system evolve according to a stochastic Markov kernel  $\mathbf{x}_t \sim \mathcal{T}(\cdot | \mathbf{x}_{t-1})$ , where  $\mathcal{T}(\cdot | \mathbf{x}) \in \mathcal{P}(\mathbb{R}^n)$  is an arbitrary conditional distribution (no assumptions on structure or modality). Let  $\mu_t$  denote the marginal of  $\mathbf{x}_t$ . Since the ground truth comes from a distribution, we measure the prediction error using the 2-Wasserstein distance  $\mathcal{E}_t = W_2(\mu_t, \hat{\mu}_t)$ , where

$\hat{\mu}_t$  is the surrogate marginal at step  $t$ . For two probability measures  $\mu, \nu \in \mathcal{P}_2(\mathbb{R}^n)$  with finite second moments, the 2-Wasserstein distance is defined as

$$W_2(\mu, \nu) = \left( \inf_{\pi \in \Pi(\mu, \nu)} \int_{\mathbb{R}^n \times \mathbb{R}^n} \|\mathbf{x} - \mathbf{y}\|^2 d\pi(\mathbf{x}, \mathbf{y}) \right)^{1/2}, \quad (18)$$

where  $\Pi(\mu, \nu)$  denotes the collection of all joint probability measures (couplings) on  $\mathbb{R}^n \times \mathbb{R}^n$  with marginals  $\mu$  and  $\nu$ . Now, we define the *intrinsic spread* of  $\mathcal{T}$ ,

$$V^* = \sup_{\mathbf{x}} \inf_{\mathbf{y} \in \mathbb{R}^n} W_2(\mathcal{T}(\cdot | \mathbf{x}), \delta_{\mathbf{y}}), \quad (19)$$

as the best-possible  $W_2$  distance from  $\mathcal{T}(\cdot | \mathbf{x})$  to any point mass, where  $\delta_{\mathbf{y}}$  denotes the Dirac measure centered at  $\mathbf{y}$ . Because the 2-Wasserstein distance to a Dirac mass is minimized exactly at the distribution's mean [43], the inner infimum evaluates to the square root of the total variance:

$$\inf_{\mathbf{y} \in \mathbb{R}^n} W_2^2(\mathcal{T}(\cdot | \mathbf{x}), \delta_{\mathbf{y}}) = \mathbb{E}_{\mathbf{z} \sim \mathcal{T}(\cdot | \mathbf{x})} [\|\mathbf{z} - \mathbb{E}[\mathbf{z}]\|^2] = \text{Tr}(\text{Var}(\mathcal{T}(\cdot | \mathbf{x}))).$$

This makes  $V^*$  a fundamental property of the true dynamics:  $V^* > 0$  for any non-degenerate kernel (where the variance is strictly positive for at least one state  $\mathbf{x}$ ) and is naturally large when  $\mathcal{T}$  is multimodal.

Now, we reintroduce the surrogate models used to approximate  $\mathcal{T}$ . Let  $S_\theta : \mathbb{R}^n \rightarrow \mathbb{R}^n$  denote a deterministic surrogate mapping and  $p_\theta(\cdot | \mathbf{x}) \in \mathcal{P}_2(\mathbb{R}^n)$  denote a probabilistic surrogate transition kernel, both parameterized by  $\theta$ . We compare two surrogate classes where  $\mathbf{x}'$  is a free dummy variable.

- **Deterministic:**  $\hat{\mathbf{x}}_t = S_\theta(\hat{\mathbf{x}}_{t-1})$ , with Lipschitz constant  $L_{det} = \sup_{\mathbf{x} \neq \mathbf{x}'} \|S_\theta(\mathbf{x}) - S_\theta(\mathbf{x}')\| / \|\mathbf{x} - \mathbf{x}'\|$ .
- **Probabilistic:**  $\hat{\mathbf{x}}_t \sim p_\theta(\cdot | \hat{\mathbf{x}}_{t-1})$ , with Wasserstein-Lipschitz constant  $L_{prob} = \sup_{\mathbf{x} \neq \mathbf{x}'} W_2(p_\theta(\cdot | \mathbf{x}), p_\theta(\cdot | \mathbf{x}')) / \|\mathbf{x} - \mathbf{x}'\|$ .

Both surrogates share the initial condition  $\hat{\mu}_0 = \mu_0$ , so  $\mathcal{E}_0 = 0$ .

### One-Step Error

The one-step mismatch of each surrogate is the  $W_2$  distance between the true kernel and the surrogate kernel, evaluated at the *same* conditioning state:

$$\epsilon_{det} = \sup_{\mathbf{x}} W_2(\mathcal{T}(\cdot | \mathbf{x}), \delta_{S_\theta(\mathbf{x})}), \quad (20)$$

$$\epsilon_{prob} = \sup_{\mathbf{x}} W_2(\mathcal{T}(\cdot | \mathbf{x}), p_\theta(\cdot | \mathbf{x})). \quad (21)$$

Here, the deterministic prediction  $S_\theta(\mathbf{x})$  is lifted to a probability measure via the Dirac delta  $\delta_{S_\theta(\mathbf{x})}$  to compute the Wasserstein distance [43], whereas  $p_\theta(\cdot | \mathbf{x})$  is inherently a valid distribution. By the definition of  $V^*$  and as shown above, the deterministic mismatch satisfies  $\epsilon_{det} \geq V^* > 0$  for *any*  $S_\theta$ . The probabilistic mismatch satisfies  $\epsilon_{prob} \rightarrow 0$  as  $p_\theta \rightarrow \mathcal{T}$ : that is, it can be made arbitrarily small given sufficient model capacity and optimal training [43].

### Autoregressive Error Bound

**Proposition 3.1.** *For a chaotic surrogate model with a one-step error  $\epsilon \in \{\epsilon_{det}, \epsilon_{prob}\}$  and the Wasserstein-Lipschitz constant  $L > 1$ , where  $L \in \{L_{det}, L_{prob}\}$ , the prediction error satisfies*

$$\mathcal{E}_t \leq \frac{e^{\Lambda T} - 1}{\Lambda} \bar{\epsilon}, \quad \Lambda = \frac{\ln L}{\Delta t}, \quad \bar{\epsilon} = \frac{\epsilon}{\Delta t}, \quad T = t\Delta t. \quad (22)$$

*Proof.* Let  $(\mathbf{x}_{t-1}, \hat{\mathbf{x}}_{t-1})$  be an optimal  $W_2$ -coupling of  $(\mu_{t-1}, \hat{\mu}_{t-1})$ . Drawing  $\mathbf{x}_t \sim \mathcal{T}(\cdot | \mathbf{x}_{t-1})$  and  $\hat{\mathbf{x}}_t$  from the surrogate kernel, coupled optimally given  $(\mathbf{x}_{t-1}, \hat{\mathbf{x}}_{t-1})$ , yields a valid (suboptimal) coupling of  $(\mu_t, \hat{\mu}_t)$ . The  $W_2$  triangle inequality then gives

$$\mathcal{E}_t \leq \underbrace{W_2(\mathcal{T}(\cdot | \mathbf{x}_{t-1}), p_\theta(\cdot | \mathbf{x}_{t-1}))}_{\leq \epsilon} + \underbrace{W_2(p_\theta(\cdot | \mathbf{x}_{t-1}), p_\theta(\cdot | \hat{\mathbf{x}}_{t-1}))}_{\leq L \mathcal{E}_{t-1}}, \quad (23)$$

where the first term uses the definition of  $\epsilon$  and the second uses the Wasserstein-Lipschitz property pointwise:  $W_2(p_\theta(\cdot | \mathbf{x}), p_\theta(\cdot | \mathbf{x}')) \leq L \|\mathbf{x} - \mathbf{x}'\|$ , which upon integrating against the optimal coupling of  $(\mu_{t-1}, \hat{\mu}_{t-1})$  and applying

the Cauchy-Schwarz inequality gives  $\mathbb{E}[L\|\mathbf{x}_{t-1} - \hat{\mathbf{x}}_{t-1}\|] \leq L\mathcal{E}_{t-1}$ . We get the recursion  $\mathcal{E}_t \leq L\mathcal{E}_{t-1} + \epsilon$  with  $\mathcal{E}_0 = 0$ . Unrolling over  $t$  steps (similar to Chakraborty et al. [83]),

$$\mathcal{E}_t \leq \epsilon \sum_{k=0}^{t-1} L^k = \epsilon \frac{L^t - 1}{L - 1}. \quad (24)$$

Writing  $L^t = e^{\Lambda t}$  and bounding  $L - 1 \geq \Lambda \Delta t$  (since  $e^x - 1 \geq x$ ) yields Equation (22). The  $L > 1$  is typically justified for chaotic systems [84, 85]. (Note : In the case where  $L = 1$  (i.e.,  $\Lambda = 0$ ), the bound reduces via L'Hôpital's rule to  $\mathcal{E}_t \leq T\bar{\epsilon} = t\epsilon$ , showing linear error growth.)  $\square$

Applying Proposition 3.1 to each surrogate gives the two explicit bounds:

$$\mathcal{E}_t^{det} \leq \frac{e^{\Lambda_{det} T} - 1}{\Lambda_{det}} \bar{\epsilon}_{det}, \quad \bar{\epsilon}_{det} \geq \bar{V}^* = \frac{V^*}{\Delta t} > 0, \quad (25)$$

$$\mathcal{E}_t^{prob} \leq \frac{e^{\Lambda_{prob} T} - 1}{\Lambda_{prob}} \bar{\epsilon}_{prob}, \quad \bar{\epsilon}_{prob} \rightarrow 0 \text{ as } p_\theta \rightarrow \mathcal{T}. \quad (26)$$

**Remark:** The two bounds differ in both factors. The per-step error  $\bar{\epsilon}_{det}$  is bounded away from zero by  $\bar{V}^*$  for any deterministic model, while  $\bar{\epsilon}_{prob}$  is fully reducible. The growth rates  $\Lambda_{det}$  and  $\Lambda_{prob}$  reflect the smoothness of each surrogate model (similar to the Jacobian of the hybrid solver in Chakraborty et al. [83]), respectively. In a typical scenario where both models can approximately capture the underlying dynamical systems, these growth rates should be very similar. This can make the per-step error a determining factor for a long-term accurate surrogate model. Further neural architecture research in this area can be guided towards minimizing these error terms.

### 3.2 Diffusion Posterior Sampling with Sparse Sensors

We show that for an arbitrary prior  $p(\mathbf{x}_0)$  with  $\mathbb{E}[\|\mathbf{x}_0\|^2] < \infty$ , the reconstruction error equals the expected posterior uncertainty, adding sensors always reduces this error, and that placing the next sensor at the highest-uncertainty node maximizes the guaranteed minimum per-step reduction. We also connect these optimal strategies with our heuristic sensor placement strategies in Section 2.5.

**Setup.** Consider an observed realization of the ground-truth  $\mathbf{x}_0 \in \mathbb{R}^N$  with  $\mathbb{E}[\|\mathbf{x}_0\|^2] < \infty$  on a mesh of  $N$  nodes (considering a single variable for simplicity). A configuration of  $s \leq N$  sensors is encoded by a linear measurement operator  $M : \mathbb{R}^N \rightarrow \mathbb{R}^s$ , selecting rows indexed by  $\mathcal{S}_s \subset \{1, \dots, N\}$ . Observations follow

$$\mathbf{y}_s = M\mathbf{x}_0 + \boldsymbol{\eta}, \quad \boldsymbol{\eta} \sim \mathcal{N}(\mathbf{0}, \sigma_\eta^2 \mathbf{I}_s), \quad (27)$$

where  $\sigma_\eta^2 > 0$ . Let  $\hat{\mathbf{x}}_s = \mathbb{E}[\mathbf{x}_0 | \mathbf{y}_s]$  be the MMSE (Minimum mean Square Error) estimate and

$$\mathcal{E}(s) = \mathbb{E}[\|\mathbf{x}_0 - \hat{\mathbf{x}}_s\|^2] \quad (28)$$

the mean-squared reconstruction error.

**MSE equals expected posterior uncertainty.** Since  $\hat{\mathbf{x}}_s = \mathbb{E}[\mathbf{x}_0 | \mathbf{y}_s]$ , the residual  $\mathbf{x}_0 - \hat{\mathbf{x}}_s$  is the posterior fluctuation around the conditional mean. Writing  $\|\mathbf{v}\|^2 = \text{Tr}(\mathbf{v}\mathbf{v}^\top)$  and interchanging trace and expectation,

$$\mathcal{E}(s) = \text{Tr}\left(\mathbb{E}[(\mathbf{x}_0 - \hat{\mathbf{x}}_s)(\mathbf{x}_0 - \hat{\mathbf{x}}_s)^\top]\right).$$

Applying the tower property,  $\mathbb{E}[(\mathbf{x}_0 - \hat{\mathbf{x}}_s)(\mathbf{x}_0 - \hat{\mathbf{x}}_s)^\top] = \mathbb{E}[\text{Var}(\mathbf{x}_0 | \mathbf{y}_s)]$  by definition of conditional covariance, we obtain

$$\mathcal{E}(s) = \text{Tr}\left(\mathbb{E}[\text{Var}(\mathbf{x}_0 | \mathbf{y}_s)]\right) = \mathbb{E}\left[\text{Tr}(\text{Var}(\mathbf{x}_0 | \mathbf{y}_s))\right]. \quad (29)$$

The MSE is therefore the *expected total posterior variance*, in conjunction with the A-optimality criterion of classical optimal experimental design [9, 7, 8].

**Proposition 3.2** (Monotone reduction with sensor count). *Let  $\mathcal{S}_1 \subset \mathcal{S}_2 \subset \dots \subset \{1, \dots, N\}$  be a nested sequence of index sets, where  $M_{s+1}$  extends  $M_s$  by adding a single sensor at node  $i$ . Then*

$$\Delta_i := \mathcal{E}(s) - \mathcal{E}(s+1) = \mathbb{E}\left[\text{Tr}(\text{Var}(\mathbf{x}_0 | \mathbf{y}_s) - \text{Var}(\mathbf{x}_0 | \mathbf{y}_{s+1}))\right] = \mathbb{E}[\|\hat{\mathbf{x}}_{s+1} - \hat{\mathbf{x}}_s\|^2] \geq 0, \quad (30)$$

so  $\mathcal{E}(s+1) \leq \mathcal{E}(s)$  for all  $s < N$ .

*Proof.* Since  $\mathbf{y}_s$  is a sub-vector of  $\mathbf{y}_{s+1}$ , the matrix law of total variance applied to  $(\mathbf{x}_0, \mathbf{y}_s, \mathbf{y}_{s+1})$  gives

$$\text{Var}(\mathbf{x}_0 | \mathbf{y}_s) = \mathbb{E}[\text{Var}(\mathbf{x}_0 | \mathbf{y}_{s+1}) | \mathbf{y}_s] + \text{Var}(\hat{\mathbf{x}}_{s+1} | \mathbf{y}_s). \quad (31)$$

Both summands on the right are positive-semidefinite. Taking trace and unconditional expectations and applying Equation 29 at both stages:

$$\mathcal{E}(s) = \mathcal{E}(s+1) + \mathbb{E}[\text{Tr}(\text{Var}(\hat{\mathbf{x}}_{s+1} | \mathbf{y}_s))].$$

By the tower property,  $\mathbb{E}[\hat{\mathbf{x}}_{s+1} | \mathbf{y}_s] = \mathbb{E}[\mathbb{E}[\mathbf{x}_0 | \mathbf{y}_{s+1}] | \mathbf{y}_s] = \mathbb{E}[\mathbf{x}_0 | \mathbf{y}_s] = \hat{\mathbf{x}}_s$ , so

$$\mathbb{E}[\text{Tr}(\text{Var}(\hat{\mathbf{x}}_{s+1} | \mathbf{y}_s))] = \mathbb{E}[\|\hat{\mathbf{x}}_{s+1} - \hat{\mathbf{x}}_s\|^2] \geq 0,$$

which gives Equation 30.  $\square$

**Justification for uncertainty-guided placement.** We write  $u_i^2 := \text{Var}(x_{0,i})$  for the prior marginal variance at node  $i$  (for example, estimated directly from the diffusion ensemble without sensors). We show that  $u_i$  is the right criterion for the first placement and a reasonable proxy for subsequent placements.

*One-step guarantee.* At any stage  $s$ , let the expected posterior variance be denoted by  $v_i^2 := \mathbb{E}[\text{Var}(x_{0,i} | \mathbf{y}_s)]$ . By the scalar law of total variance applied to each coordinate  $j$ ,

$$v_j^2 = \mathbb{E}[\text{Var}(x_{0,j} | \mathbf{y}_{s+1})] + \mathbb{E}[\text{Var}(\hat{x}_{s+1,j} | \mathbf{y}_s)],$$

so every term  $v_j^2 - \mathbb{E}[\text{Var}(x_{0,j} | \mathbf{y}_{s+1})] \geq 0$ . Since  $\Delta_i = \sum_{j=1}^N (v_j^2 - \mathbb{E}[\text{Var}(x_{0,j} | \mathbf{y}_{s+1})])$  (expanding the trace in Equation 30) is a sum of non-negative terms that dominates any single one,

$$\Delta_i \geq v_i^2 - \mathbb{E}[\text{Var}(x_{0,i} | \mathbf{y}_{s+1})]. \quad (32)$$

For fixed  $\mathbf{y}_s$ , by definition the MMSE of  $x_{0,i}$  from  $y_{s+1,i} = x_{0,i} + \eta_i$  cannot be worse than the linear (Wiener-filter) estimator [86], whose conditional MSE equals  $\sigma_\eta^2 V_s / (\sigma_\eta^2 + V_s)$  with  $V_s = \text{Var}(x_{0,i} | \mathbf{y}_s)$ :

$$\mathbb{E}[\text{Var}(x_{0,i} | \mathbf{y}_{s+1}) | \mathbf{y}_s] \leq \frac{\sigma_\eta^2 V_s}{\sigma_\eta^2 + V_s}.$$

Taking unconditional expectations and applying Jensen's inequality to the concave map  $k \mapsto \sigma_\eta^2 k / (\sigma_\eta^2 + k)$  (whose second derivative is  $-2\sigma_\eta^4 / (\sigma_\eta^2 + k)^3 < 0$ ):

$$\mathbb{E}[\text{Var}(x_{0,i} | \mathbf{y}_{s+1})] \leq \mathbb{E}\left[\frac{\sigma_\eta^2 V_s}{\sigma_\eta^2 + V_s}\right] \leq \frac{\sigma_\eta^2 v_i^2}{\sigma_\eta^2 + v_i^2},$$

and substituting into (32) gives

$$\Delta_i \geq \frac{v_i^4}{\sigma_\eta^2 + v_i^2}. \quad (33)$$

The right-hand side is zero if and only if  $v_i = 0$  and strictly increases for  $v_i > 0$ , so  $\arg \max_{i \notin \mathcal{S}_s} v_i$  maximizes the minimum guaranteed reduction in error. There are several additional optimization techniques that can be performed during online implementation to increase "information-gain" with added sensors [7, 87, 88, 9]. These come with added computational costs magnified for high-dimensional systems with a long time horizon of interest.

In the first step ( $s = 0$ ), the proxy is exact ( $v_i = u_i$ ). Placing the first sensor at  $\arg \max_i u_i$  is guaranteed to maximize the minimum reduction in error. For  $s \geq 1$  the bound requires the posterior quantity  $v_i$ , which our method approximates by the prior  $u_i$ . Ideally, the posterior uncertainty can also be computed by generating a new ensemble after placing each sensor, but this is computationally very expensive for a large number of sensors.

Two properties *motivate* this heuristic substitution:

1. *Conservativeness.* By the law of total variance,  $u_i^2 = v_i^2 + \text{Var}(\mathbb{E}[x_{0,i} | \mathbf{y}_s]) \geq v_i^2$ , so a node with low prior variance necessarily has low posterior variance, yields a small guaranteed  $\Delta_i$  via (33), and is not prioritized correctly.
2. *Suppression distance.* The topology-aware selection (Section 2.5) removes all candidates within a gap  $g$  of existing sensors. Intuitively, the posterior variance is likely to be reduced relative to the prior for the nodes near a sensor. Among the remaining eligible nodes,  $v_i \approx u_i$  and the prior ranking is a reasonable proxy for the posterior ranking.

**Learned error predictor as a lightweight alternative.** The identity  $\mathbb{E}[(x_{0,i} - \hat{x}_{s,i})^2] = \mathbb{E}[\text{Var}(x_{0,i} | \mathbf{y}_s)]$  (from Equation 29) means that any estimator of the per-node squared reconstruction error is a proxy for the posterior variance governing placement. During training, the spatial squared error (Equation 15) provides a node-level proxy for the uncertainty in the reconstruction. Because the diffusion network is conditioned on prior noise rather than sensor observations, the error prediction network is a heuristic approximation of the ensemble variance used in uncertainty-guided placement. This proxy is compatible with the suppression-distance strategy and provides a computationally inexpensive way to approximate uncertainty-guided placement without running an ensemble.

## 4 Results

### 4.1 Case 1: Two-dimensional turbulence

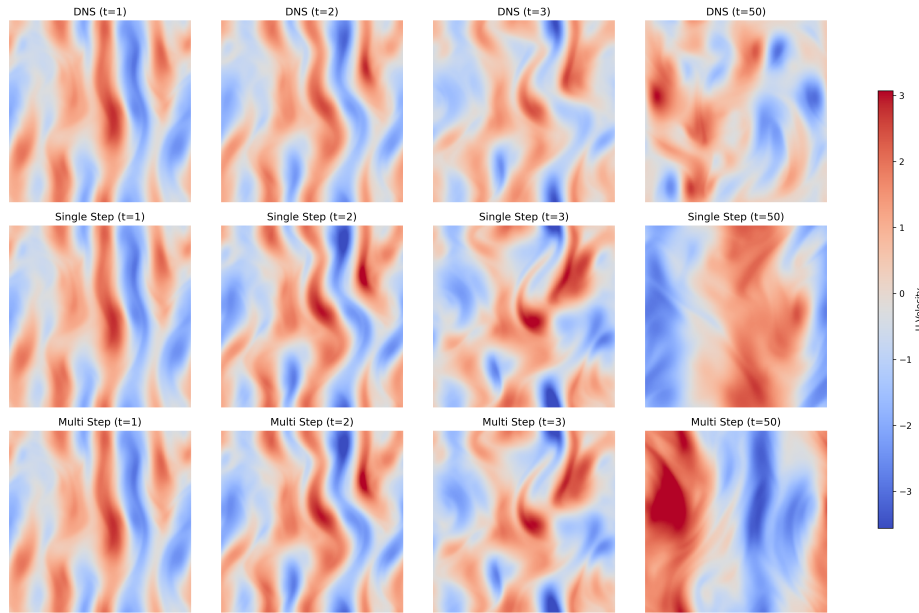


Figure 1: U velocity at different timesteps of forecast for single-step vs multi-step diffusion training along with the DNS ground truth.

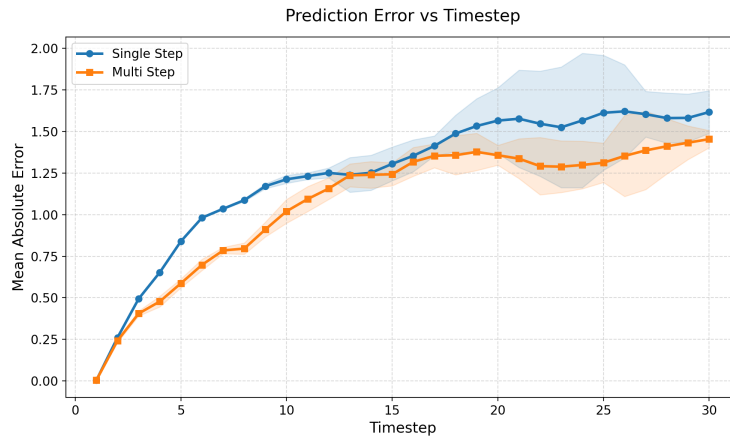


Figure 2: Mean absolute error from DNS at different timesteps of forecast for single-step vs multi-step diffusion training.

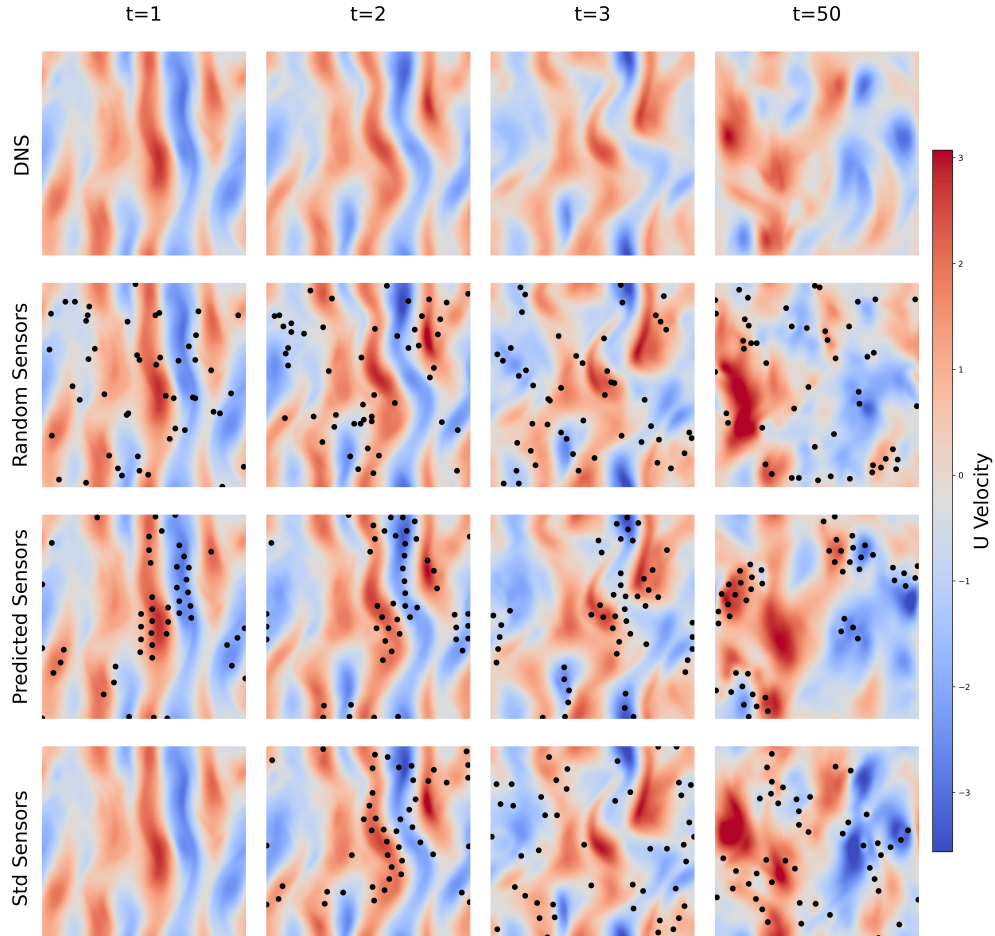


Figure 3: U velocity at different timesteps of forecast for different sensor placement techniques. The sensor locations are shown as black dots.

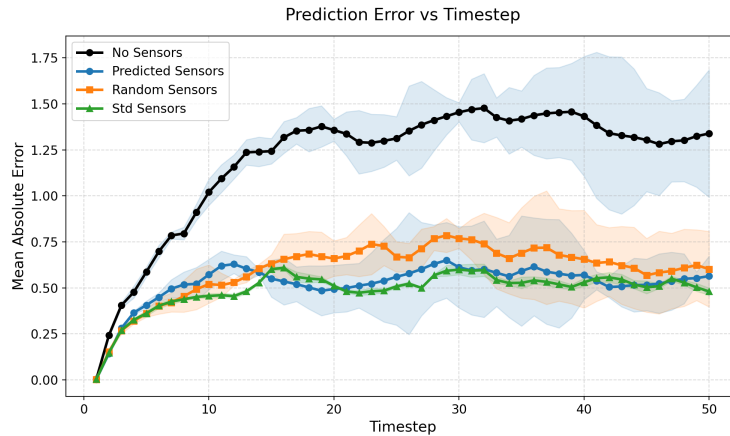


Figure 4: Mean absolute error from DNS at different timesteps of forecast for different sensor placement techniques. Sensor placements improve the forecast. These values are for 50 sensor points with a minimum distance of 15 grid points between them.

The forced two-dimensional turbulence serves as a widely adopted benchmark in the forecasting of chaotic dynamical systems [89, 90, 91]. We utilize a 2D homogeneous isotropic turbulent flow subjected to Kolmogorov forcing for building our diffusion forecast surrogate model. This system is dictated by the incompressible Navier-Stokes equations:

$$\begin{aligned} \frac{\partial \mathbf{u}}{\partial t} + \nabla \cdot (\mathbf{u} \otimes \mathbf{u}) &= \frac{1}{Re} \nabla^2 \mathbf{u} - \frac{1}{\rho} \nabla p + \mathbf{f}, \\ \nabla \cdot \mathbf{u} &= 0, \end{aligned} \quad (34)$$

where  $\mathbf{u} = (u, v)$  denotes the velocity field,  $p$  stands for the pressure,  $\rho$  indicates the fluid density, and  $Re$  represents the Reynolds number. The term  $\mathbf{f}$  introduces the external forcing mechanism, formulated as:

$$\mathbf{f} = A \sin(ky) \hat{\mathbf{e}} - r \mathbf{u}, \quad (35)$$

where  $\hat{\mathbf{e}}$  is the unit vector aligned with the  $x$ -axis. Following the configuration established by [92], our experimental setup employs an amplitude of  $A = 1$ , a wavenumber of  $k = 4$ , a linear drag coefficient of  $r = 0.1$ , and a Reynolds number of  $Re = 1000$ . The simulations are initialized using a stochastically generated divergence-free velocity field [93].

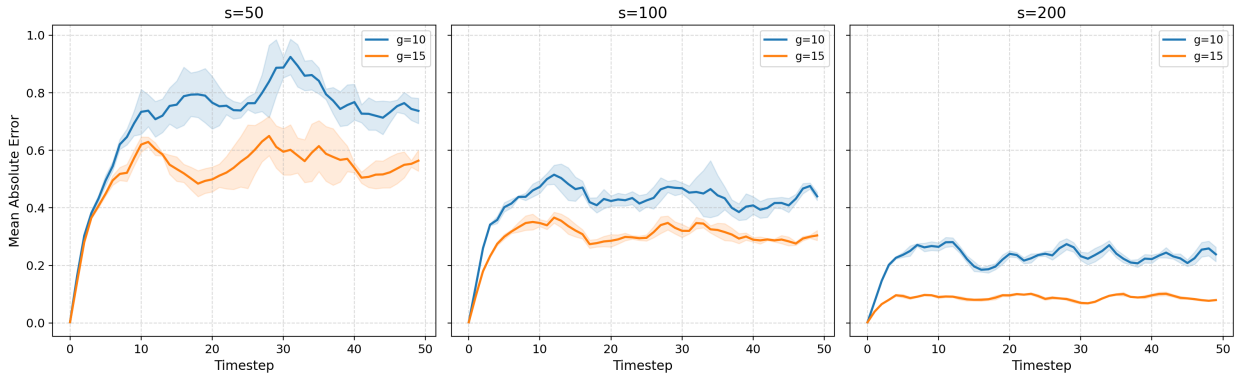


Figure 5: Plots for the mean absolute error from DNS at different timesteps of forecast for different gap between( $g$ ) and number of sensor points( $s$ ). More sensor points and larger gaps between sensors lead to lower prediction error.

To establish our ground truth datasets, we rely on direct numerical simulations (DNS) [94] applied to the governing equations. These simulations are conducted over a doubly periodic square spatial domain measuring  $L = 2\pi$ . The spatial domain is initially discretized on a uniform  $512 \times 512$  grid, which is subsequently spatially filtered to a coarser  $64 \times 64$  resolution. We extract temporal trajectory data only after the flow has fully transitioned into its chaotic regime. To guarantee meaningful variations between successive observations, flow snapshots are recorded at intervals of  $T = 256 \Delta t_{DNS}$ . For a more comprehensive breakdown of the dataset generation pipeline, readers are directed to [92]. The model and training hyperparameters are mentioned in Appendix A.

Firstly we compare the performance of single-step vs multi-step trained diffusion models. Figure 1 shows that both surrogate models can capture the ground truth reasonably well in shorter timespans and then diverge due to chaos. However, Figure 2 clearly shows that the multi-step diffusion model has a lower error. Therefore, we used the multi-step diffusion model hereafter for the rest of our experiments.

We also show the different sensor placement techniques in Figure 3. It is evident that both the predicted sensors and the standard deviation based sensors select the points based on the coherent structures of the flow field. Beyond identifying coherent structures, Figure 3 also shows that the selected sensor locations evolve with time, indicating that the proposed strategy is genuinely adaptive rather than tied to a fixed set of spatial hot spots. As a quantitative assessment, we plot the mean absolute error of the surrogate forecast from the ground truth in Figure 4. The standard deviation based sensor placement seems to perform the best among the three sensor placement techniques, although marginally in this case. We expect this because it is a homogeneous isotropic case where each point in the field is no different from any other point. Moreover, from Figure 5 we conclude that increasing the number of sensors points( $s$ ) and increasing the gap( $g$ ) between those sensors reduces the forecast error. Secondly, we observe in Figure 6 that when the gap is less ( $g=10$ ) for more sensor points ( $s=100,200$ ), the sensor placement using the predictive-model-based approach performs worse. This is because the sensors cluster in regions of high error, and even a random sensor placement can recover more information.

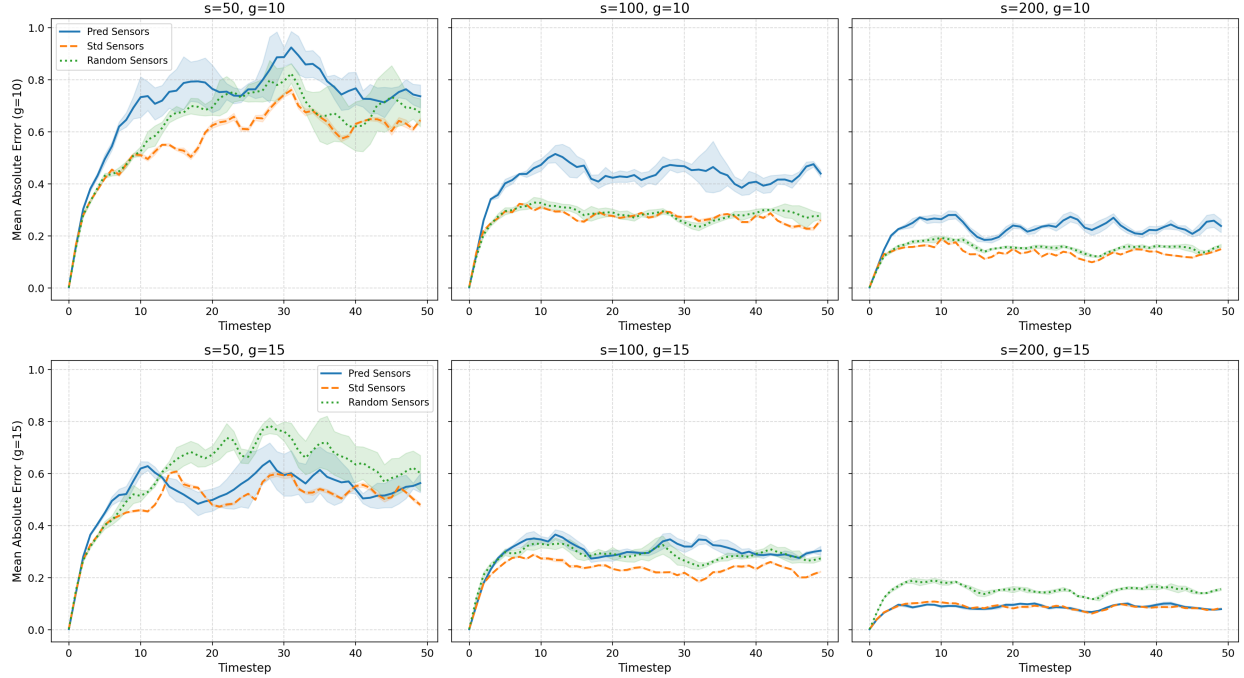


Figure 6: Plots for comparing different sensor placement techniques and their mean absolute error from DNS at different timesteps of forecast for different distance between( $d$ ) and number of sensor points( $s$ ). Standard-deviation-based sensor placement gives lowest error.

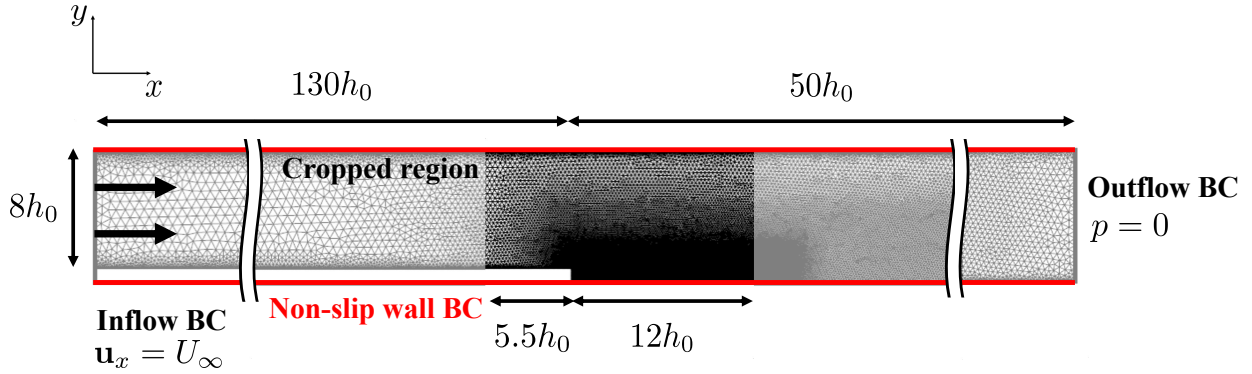


Figure 7: Visualization of the two-dimensional backwards-facing step computational domain, including boundary conditions and the cropped region used for training

## 4.2 Case 2: Flow over a backwards facing step

Flow over a backwards-facing step (BFS) is a widely studied benchmark problem in fluid dynamics, encompassing both experimental and computational approaches [95]. BFS flow is characterized by flow separation at the step and subsequent reattachment downstream, resulting in a recirculation region near the step and transient vortex shedding. These phenomena are prevalent in more complex, non-idealized flows and pose challenges in accurate modeling. Therefore, BFS serves as a valuable case study for evaluating modeling approaches. Similar to the forced two-dimensional turbulence case, BFS flow is governed by the incompressible Navier-Stokes equations as in Eq. 34. A schematic of the computational domain is presented in Fig. 7.

Based on this configuration, a large eddy simulation (LES) under the Reynolds number,  $Re = U_\infty h_{step} / \nu = 26,000$ , is performed using the finite element method (FEM) to generate the ground truth dataset, and the Smagorinsky model

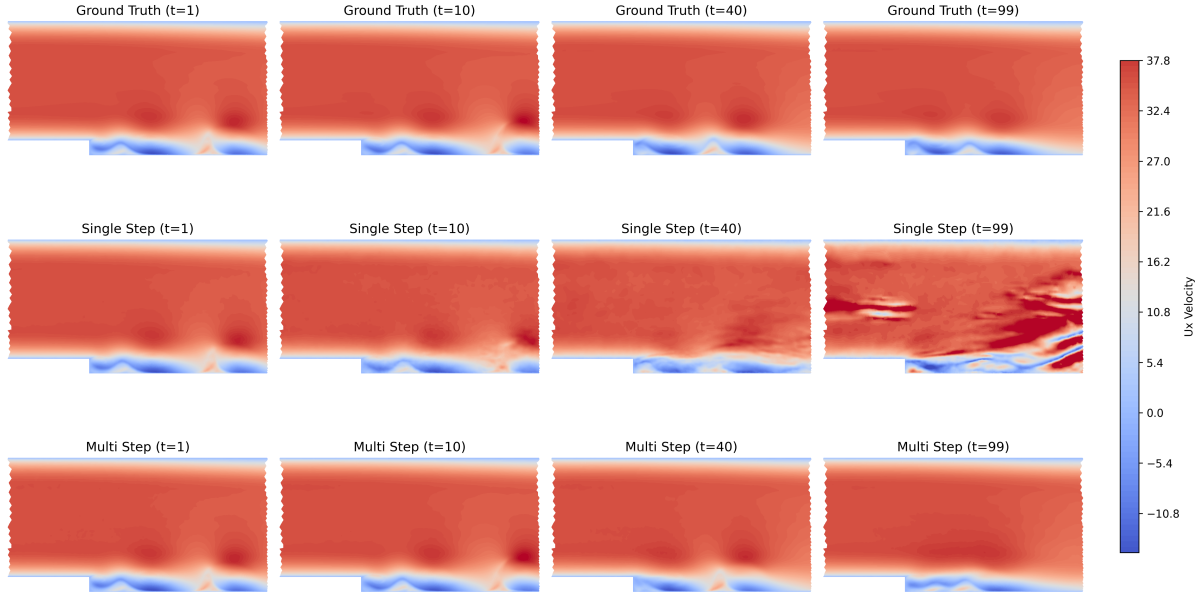


Figure 8: U velocity plots at different timesteps of forecast for single-step vs multi-step diffusion training along with the ground truth.

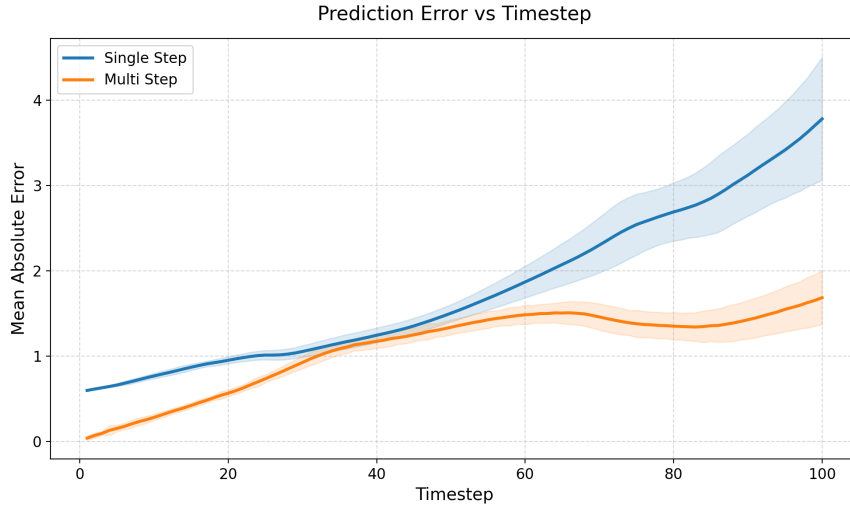


Figure 9: Mean absolute error from ground truth at different timesteps of forecast for single-step vs multi-step diffusion training.

[96] with  $C_s = 0.06$  is used for the subgrid-scale stress (SGS) model. For the FEM solver, FEniCSx [97] is used. The total grid for the two-dimensional BFS consists of 5,253 triangular Taylor-hood elements with local refinement near the step and the walls. Even though the simulation is run with the full domain, to efficiently reduce the training time and GPU memory usage, only the flowfield in the cropped subdomain near the step anchor is used as the training dataset as in Fig. 7. The timestep for the simulation is set to  $\Delta t = 1 \times 10^{-4} s$ , which is sufficient to keep the CFL number less than 1. Snapshots of the velocity field are saved every  $10^{-4}$  seconds, and a total of 800 snapshots are generated. The first 100 steps are discarded to remove initial transient effects, and the remaining 700 steps are used as the training dataset. Due to the unstructured nature of this problem we utilize the graph neural network architecture mentioned in Section 2.4. Further details on the model, training and sampling hyperparameters are mentioned in Appendix A.

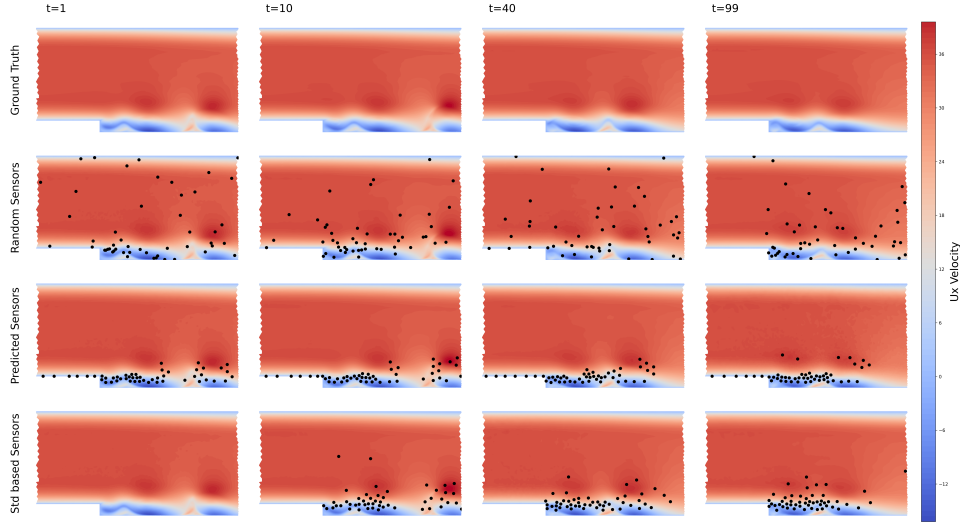


Figure 10: U velocity plots at different timesteps of forecast for different sensor placement techniques. The sensor locations are shown as black dots.

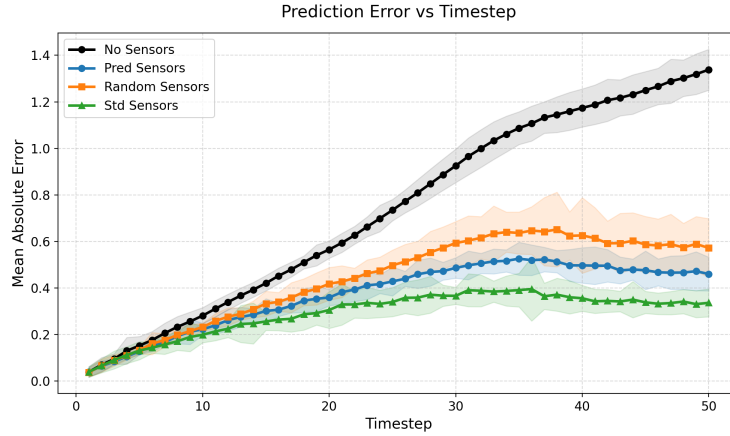


Figure 11: Mean absolute error from ground truth at different timesteps of forecast for different sensor placement techniques. Sensor placements improves the forecast. These values are for 50 sensor points with a minimum distance of 7 grid points between them.

First, we compare the single-step trained model with the multi-step trained diffusion model. We clearly observe in Figures 8 and 9 that the single-step trained diffusion model is unstable in longer rollouts. Due to this, we use the multi-step trained diffusion model for the rest of this study. Secondly, Figure 10 shows that both the predicted sensor placement and the standard deviation based sensor placement pick points near the step, which is the most turbulent part of the flow. Figure 11 also shows that the standard deviation and predicted sensor placement have lower errors than random sensor placement and no sensor placement, which was not evident in the homogeneous isotropic turbulence case. This is because of the presence of localized structures in the flow that are not captured in the random sensor placement.

In this case, we observed from Figure 12 that larger gaps( $g=7$ ) help when the number of sensor points is low( $s=20$ ). When the number of sensor points is larger ( $s=50,100$ ), a smaller gap ( $g=5$ ) has lower errors. This is because errors are more localized and a larger gap does not help by making sensors more distributed. This is opposite to what we observed

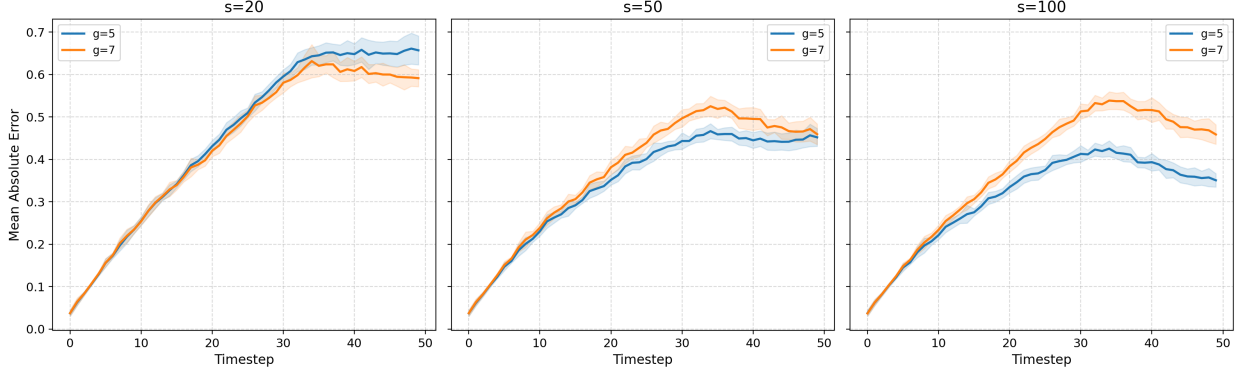


Figure 12: Plots for the mean absolute error from ground truth at different timesteps of forecast for different gap( $g$ ) and number of sensor points( $s$ ).

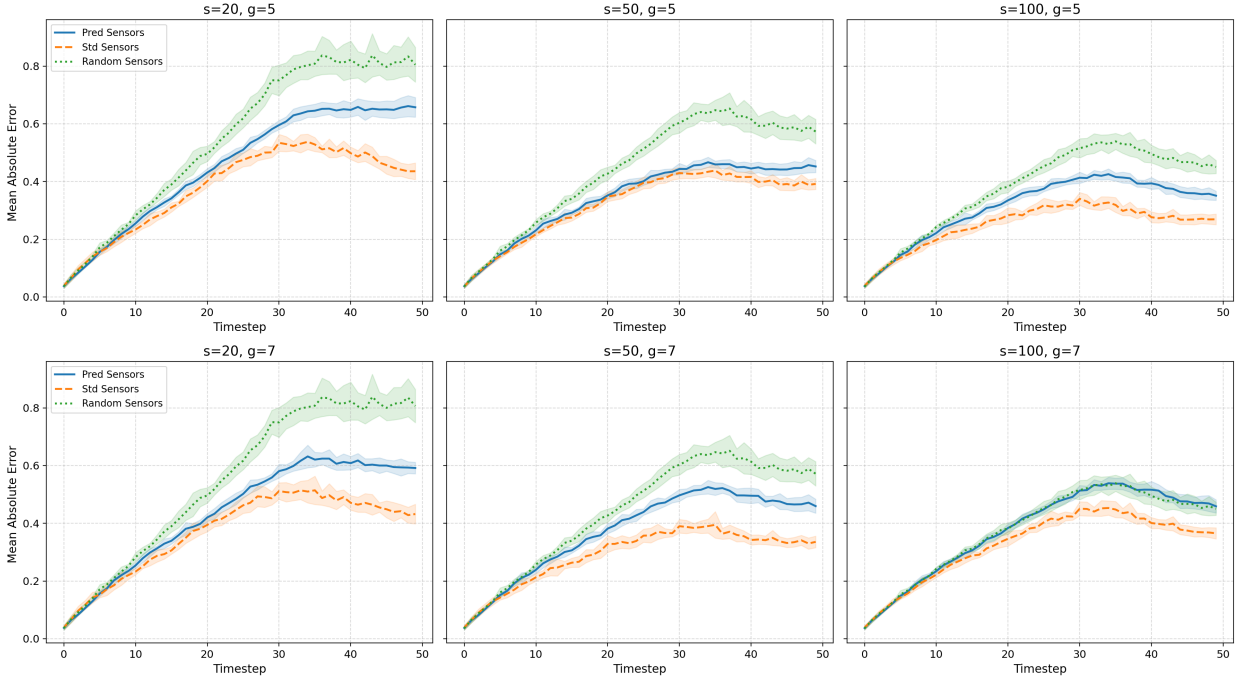


Figure 13: Plots for comparing different sensor placement techniques and their mean absolute error from ground truth at different timesteps of forecast for different gap( $g$ ) and number of sensor points( $s$ ). Random sensor placement and the standard deviation based sensor placement give the highest and lowest error respectively.

in the homogeneous isotropic turbulence case. Moreover, Figure 13 shows that for all cases except when the number of sensor points are too high ( $s=100$ ), the standard deviation based sensor placement performs best followed by the predicted sensor placement. Figure 13 also highlights that the gap in performance between the three sensor placement strategies reduce when the number of sensors increases.

To further evaluate the statistical consistency of the surrogate model under different sensor placement strategies, we compare the mean velocity profiles at several downstream locations in the two-dimensional BFS flow. Figure 14 shows the **(top)** streamwise mean velocity  $\langle u \rangle / U_\infty$  and **(bottom)** wall-normal mean velocity  $\langle v \rangle / U_\infty$  at  $x/H = 1.0, 4.0, 6.0,$  and  $9.0$ , obtained via temporal averaging over the rollout. The ground truth profiles exhibit the characteristic separation and reattachment behavior of BFS flow, with negative streamwise velocity near the wall at upstream stations and gradual recovery downstream. Incorporating sensor measurements improves agreement with the ground truth across

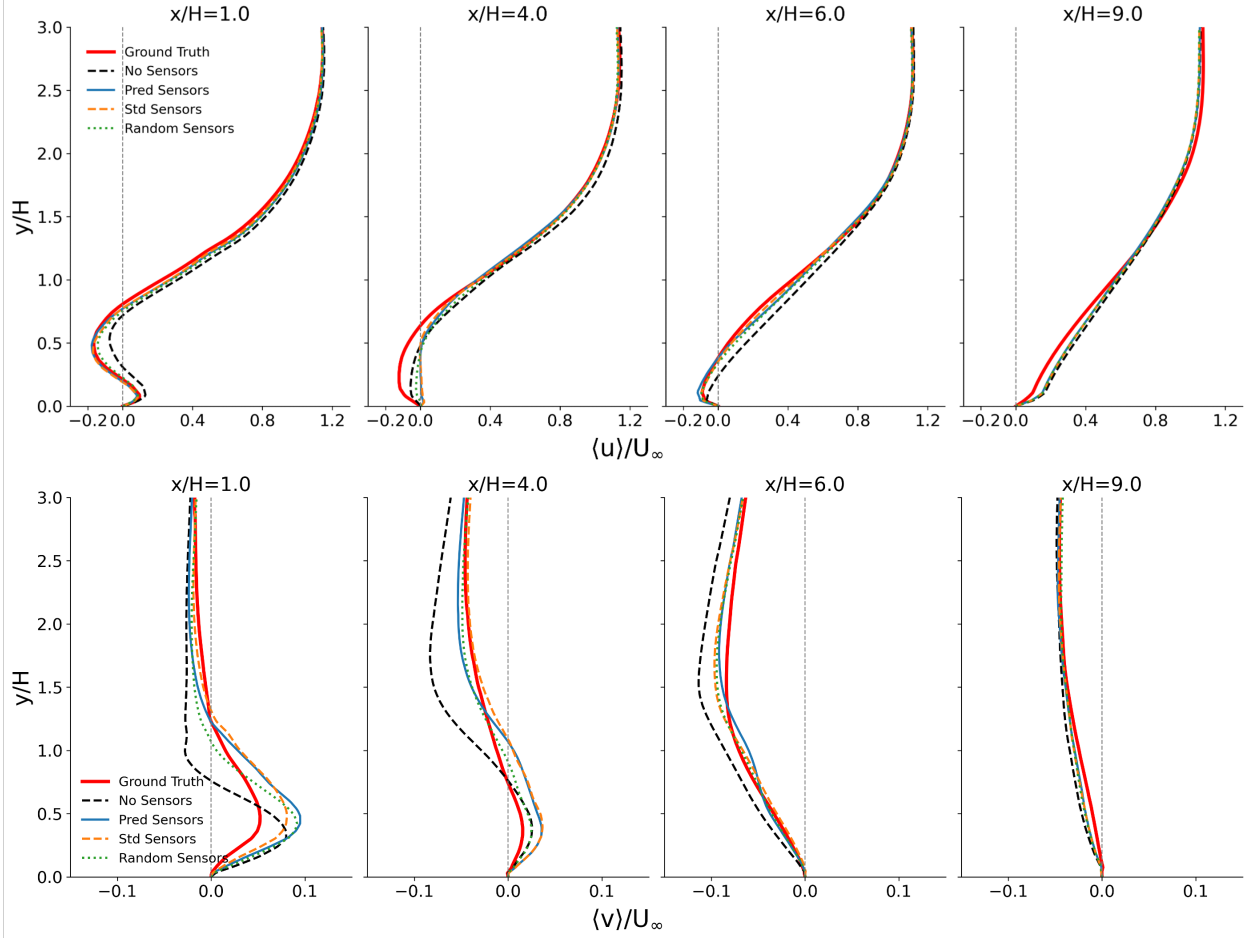


Figure 14: Predictions of the mean velocity profiles at different downstream locations of the BFS case obtained by different sensor placement techniques. **(Top)** Streamwise velocity,  $\langle u \rangle / U_\infty$ ; **(Bottom)** Wall-normal velocity,  $\langle v \rangle / U_\infty$

all downstream locations. While the differences among sensor placement strategies are relatively subtle for the mean profiles, informed placements (standard-deviation-based and predictive) generally provide slightly better reconstruction of the separated shear layer compared to random placement. Overall, the presence of sensors plays a more significant role than the specific placement strategy in recovering the key mean-flow features of the separated region.

To further assess the model’s ability to reproduce higher-order turbulence statistics, Figure 15 presents the Reynolds stress profiles at the same downstream locations. The **(top)** streamwise normal stress  $\langle u'u' \rangle / U_\infty^2$ , **(middle)** shear stress  $\langle u'v' \rangle / U_\infty^2$ , and **(bottom)** wall-normal normal stress  $\langle v'v' \rangle / U_\infty^2$  are obtained through temporal averaging. Introducing sensor measurements improves both the magnitude and spatial localization of the stress peaks. In contrast to the mean profiles, the differences among placement strategies are more discernible for the Reynolds stresses, where the standard-deviation-based placement tends to yield the closest agreement overall, followed by the predictive and random placements. Nevertheless, all sensor-informed cases show clear improvement over the no-sensor configuration.

### 4.3 Sampling Computational Costs

We compare the sampling costs for the different sensor placement techniques for homogeneous isotropic turbulence and the backwards-facing step in Figure 16. We used 1 NVIDIA A100 for the homogeneous isotropic turbulence case (ensemble size 16) and 12 Intel Data Center Max 1550 Series for the backwards-facing step case (ensemble size 12). We observe in both cases that for the model predicted sensor placement and the standard deviation based sensor placement the computational cost of sampling increases approximately linearly with number of sampling points. This is

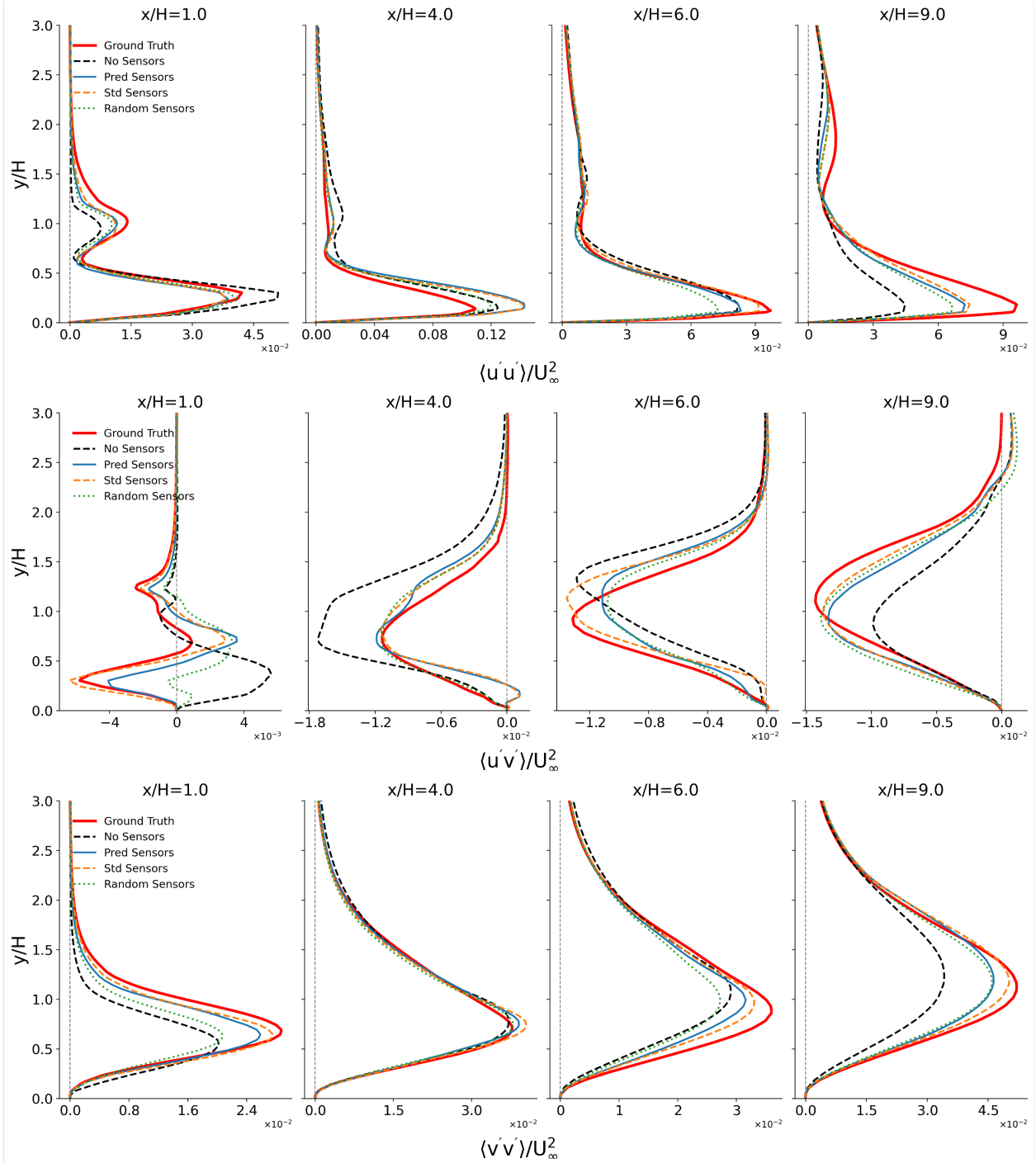


Figure 15: Predictions of the Reynolds stress profiles at different downstream locations of the BFS case obtained by different sensor placement techniques. **(Top)** Streamwise normal stress,  $\langle u'u' \rangle / U_\infty^2$ ; **(Middle)** Shear stress,  $\langle u'v' \rangle / U_\infty^2$ ; **(Bottom)** Vertical normal stress,  $\langle v'v' \rangle / U_\infty^2$ . The placement of sensors generally leads to improved prediction of stresses with the uncertainty-based placement strategy being most effective.

consistent with our greedy sensor placement technique in Section 2.5. Here, the predicted sensor placement shows similar performance to the standard deviation based sensor placement as we keep the ensemble size fixed for both cases.

However, the predicted sensor placement technique does not need any ensemble to place the sensors, which can make it ideal for a limited computational budget.

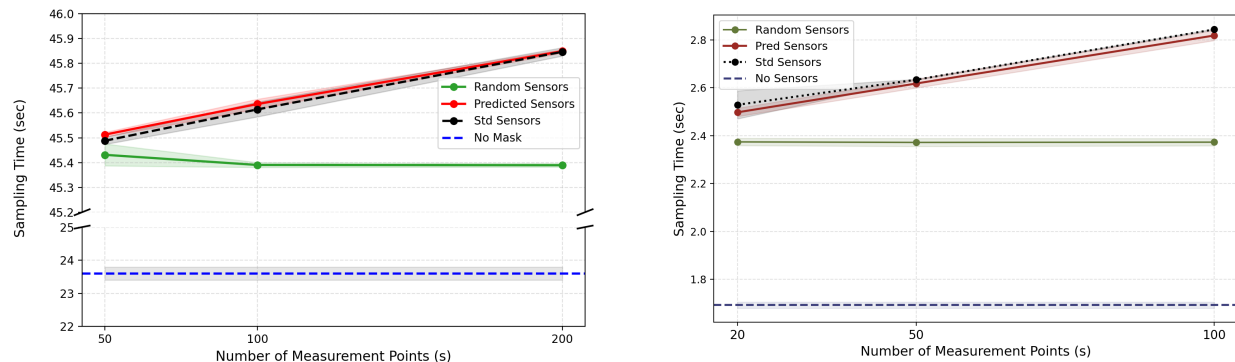


Figure 16: Relationship between the number of measurement points/sensors ( $s$ ) and the sampling time (in seconds) for various sensor placement techniques for (left) homogeneous isotropic turbulence sampling and (right) backward-facing step sampling. The shading represents uncertainty ( $\pm 3\sigma$ ) over 5 runs.

## 5 Discussions and Conclusion

We have presented a novel framework for the probabilistic forecasting of high-dimensional chaotic dynamical systems with exemplar applications such as turbulent flows. Our proposed approach uses deep learning diffusion models and provides stable long-term forecast horizons, a capacity to learn states provided on unstructured grids, and unifies Bayesian data assimilation and computationally efficient optimal sensor placement.

Through experiments on benchmark datasets given by two-dimensional turbulence and flow over a backwards facing step, we discover that a multi-step autoregressive training objective improves physical consistency and stability over long rollouts, effectively mitigating the error growth typically observed in single-step training. Additionally, we exploit the Bayesian interpretation of the diffusion model (as a training data-informed prior) to enable rapid data assimilation from sparse observations of the ground truth. Furthermore, estimates of uncertainty from the diffusion model also enable adaptive sensor placement at the cost of ensemble member generation. To mitigate this extra cost, we show that a metamodel trained to generate predictions for the parent diffusion model can also be used for efficient sensor placement decision making. In heterogeneous flows, such as the backwards-facing step, uncertainty-driven and predictive sensor placement strategies outperform random sampling by targeting specific regions that show higher degrees of turbulence and anisotropy. We also find that the introduction of topology-aware suppression is important during the sensor placement process; by enforcing spatial separation between sensors, we maximize information gain and prevent the “clustering” of measurements in localized high-error zones.

While the current work focuses on two-dimensional benchmarks, the graph-based nature of the architecture makes it inherently scalable to three-dimensional geometries and complex multi-physics problems [98]. Future work will extend this to more challenging cases and explore the integration of physics-informed constraints directly into the graph edge and node operations in the network to further enhance the conservation properties of the generated flow fields.

## 6 Acknowledgments

We acknowledge support from ARO cooperative agreement W911NF-25-2-0183 and an ARO ECP award from the Program ‘Modeling of Complex Systems’ (PM - Dr. Rob Martin). This research used resources of the Argonne Leadership Computing Facility, which is a U.S. Department of Energy Office of Science User Facility operated under Contract DE-AC02-06CH11357. We acknowledge Shraddha Pathak, College of Information Sciences and Technology, Pennsylvania State University, for reviewing the error analysis in Section 3.1. We also acknowledge computing resources from the Penn State Institute for Computational and Data Sciences.

## References

- [1] Stephen B Pope. Turbulent flows. *Measurement Science and Technology*, 12(11):2020–2021, 2001.

- [2] Jonathan Ho, Ajay Jain, and Pieter Abbeel. Denoising diffusion probabilistic models. *Advances in neural information processing systems*, 33:6840–6851, 2020.
- [3] Tero Karras, Miika Aittala, Timo Aila, and Samuli Laine. Elucidating the design space of diffusion-based generative models. *Advances in neural information processing systems*, 35:26565–26577, 2022.
- [4] Hyungjin Chung, Jeongsol Kim, Michael T Mccann, Marc L Klasky, and Jong Chul Ye. Diffusion posterior sampling for general noisy inverse problems. *arXiv preprint arXiv:2209.14687*, 2022.
- [5] François Rozet and Gilles Louppe. Score-based data assimilation. *Advances in Neural Information Processing Systems*, 36:40521–40541, 2023.
- [6] Brian Thomas Hinson. *Observability-based guidance and sensor placement*. PhD thesis, 2015.
- [7] Krithika Manohar, Bingni W Brunton, J Nathan Kutz, and Steven L Brunton. Data-driven sparse sensor placement for reconstruction: Demonstrating the benefits of exploiting known patterns. *IEEE Control Systems Magazine*, 38(3):63–86, 2018.
- [8] Yuezhou Ma, Haixu Wu, Hang Zhou, Huikun Weng, Jianmin Wang, and Mingsheng Long. Physense: Sensor placement optimization for accurate physics sensing. *arXiv preprint arXiv:2505.18190*, 2025.
- [9] Kathryn Chaloner and Isabella Verdinelli. Bayesian experimental design: A review. *Statistical science*, pages 273–304, 1995.
- [10] Shaunak D Bopardikar. A randomized approach to sensor placement with observability assurance. *Automatica*, 123:109340, 2021.
- [11] Natalie L Brace, Nicholas B Andrews, Jeremy Upsal, and Kristi A Morgansen. Sensor placement on a cantilever beam using observability gramians. In *2022 IEEE 61st Conference on Decision and Control (CDC)*, pages 388–395. IEEE, 2022.
- [12] Hojin Kim and Romit Maulik. Towards interpretable deep learning and analysis of dynamical systems via the discrete empirical interpolation method. *arXiv preprint arXiv:2510.21852*, 2025.
- [13] Seongjun Yun, Minbyul Jeong, Raehyun Kim, Jaewoo Kang, and Hyunwoo J Kim. Graph transformer networks. *Advances in neural information processing systems*, 32, 2019.
- [14] Christopher KI Williams and Carl Edward Rasmussen. *Gaussian processes for machine learning*, volume 2. MIT press Cambridge, MA, 2006.
- [15] Martin Dietrich Buhmann. Radial basis functions. *Acta numerica*, 9:1–38, 2000.
- [16] Jerome Sacks, William J Welch, Toby J Mitchell, and Henry P Wynn. Design and analysis of computer experiments. *Statistical science*, 4(4):409–423, 1989.
- [17] Alexander Forrester, Andras Sobester, and Andy Keane. *Engineering design via surrogate modelling: a practical guide*. John Wiley & Sons, 2008.
- [18] Saman Razavi, Bryan A Tolson, and Donald H Burn. Review of surrogate modeling in water resources. *Water Resources Research*, 48(7), 2012.
- [19] Zongyi Li, Nikola Kovachki, Kamyar Aizzadenesheli, Burigede Liu, Kaushik Bhattacharya, Andrew Stuart, and Anima Anandkumar. Fourier neural operator for parametric partial differential equations. *arXiv preprint arXiv:2010.08895*, 2020.
- [20] Lu Lu, Pengzhan Jin, Guofei Pang, Zhongqiang Zhang, and George Em Karniadakis. Learning nonlinear operators via deeponet based on the universal approximation theorem of operators. *Nature machine intelligence*, 3(3): 218–229, 2021.
- [21] Sepp Hochreiter, Jürgen Schmidhuber, et al. Long short-term memory [j]. *Neural computation*, 9(8):1735–1780, 1997.
- [22] Kyunghyun Cho, Bart Van Merriënboer, Caglar Gulcehre, Dzmitry Bahdanau, Fethi Bougares, Holger Schwenk, and Yoshua Bengio. Learning phrase representations using rnn encoder-decoder for statistical machine translation. *arXiv preprint arXiv:1406.1078*, 2014.
- [23] Pantelis R Vlachas, Wonmin Byeon, Zhong Y Wan, Themistoklis P Sapsis, and Petros Koumoutsakos. Data-driven forecasting of high-dimensional chaotic systems with long short-term memory networks. *Proceedings of the Royal Society A: Mathematical, Physical and Engineering Sciences*, 474(2213), 2018.
- [24] Pantelis-Rafail Vlachas, Jaideep Pathak, Brian R Hunt, Themistoklis P Sapsis, Michelle Girvan, Edward Ott, and Petros Koumoutsakos. Backpropagation algorithms and reservoir computing in recurrent neural networks for the forecasting of complex spatiotemporal dynamics. *Neural Networks*, 126:191–217, 2020.

- [25] Nicholas Geneva and Nicholas Zabaras. Transformers for modeling physical systems. *Neural Networks*, 146: 272–289, 2022.
- [26] Haixu Wu, Huakun Luo, Haowen Wang, Jianmin Wang, and Mingsheng Long. Transolver: A fast transformer solver for pdes on general geometries. *arXiv preprint arXiv:2402.02366*, 2024.
- [27] Alberto Solera-Rico, Carlos Sanmiguel Vila, Miguel Gómez-López, Yuning Wang, Abdulrahman Almashjary, Scott TM Dawson, and Ricardo Vinuesa.  $\beta$ -variational autoencoders and transformers for reduced-order modelling of fluid flows. *Nature Communications*, 15(1):1361, 2024.
- [28] Zijie Li, Dule Shu, and Amir Barati Farimani. Scalable transformer for pde surrogate modeling. *Advances in Neural Information Processing Systems*, 36:28010–28039, 2023.
- [29] Jascha Sohl-Dickstein, Eric Weiss, Niru Maheswaranathan, and Surya Ganguli. Deep unsupervised learning using nonequilibrium thermodynamics. In *International conference on machine learning*, pages 2256–2265. pmlr, 2015.
- [30] Yang Song, Jascha Sohl-Dickstein, Diederik P Kingma, Abhishek Kumar, Stefano Ermon, and Ben Poole. Score-based generative modeling through stochastic differential equations. *arXiv preprint arXiv:2011.13456*, 2020.
- [31] Prafulla Dhariwal and Alexander Nichol. Diffusion models beat gans on image synthesis. *Advances in neural information processing systems*, 34:8780–8794, 2021.
- [32] Jonathan Ho, Tim Salimans, Alexey Gritsenko, William Chan, Mohammad Norouzi, and David J Fleet. Video diffusion models. *Advances in neural information processing systems*, 35:8633–8646, 2022.
- [33] Phillip Lippe, Bas Veeling, Paris Perdikaris, Richard Turner, and Johannes Brandstetter. Pde-refiner: Achieving accurate long rollouts with neural pde solvers. *Advances in Neural Information Processing Systems*, 36:67398–67433, 2023.
- [34] Han Gao, Sebastian Kaltenbach, and Petros Koumoutsakos. Generative learning for forecasting the dynamics of high-dimensional complex systems. *Nature Communications*, 15(1):8904, 2024.
- [35] Georg Kohl, Li-Wei Chen, and Nils Thuerey. Benchmarking autoregressive conditional diffusion models for turbulent flow simulation. *Neural Networks*, page 108641, 2026.
- [36] Vivek Oommen, Aniruddha Bora, Zhen Zhang, and George Em Karniadakis. Integrating neural operators with diffusion models improves spectral representation in turbulence modeling. *arXiv preprint arXiv:2409.08477*, 2024.
- [37] Qiang Liu and Nils Thuerey. Uncertainty-aware surrogate models for airfoil flow simulations with denoising diffusion probabilistic models. *AIAA Journal*, 62(8):2912–2933, 2024.
- [38] Marten Lienen, David Lüdke, Jan Hansen-Palmus, and Stephan Günnemann. From zero to turbulence: Generative modeling for 3d flow simulation. *arXiv preprint arXiv:2306.01776*, 2023.
- [39] Kashif Rasul, Calvin Seward, Ingmar Schuster, and Roland Vollgraf. Autoregressive denoising diffusion models for multivariate probabilistic time series forecasting. In *International conference on machine learning*, pages 8857–8868. PMLR, 2021.
- [40] Han Gao, Xu Han, Xiantao Fan, Luning Sun, Li-Ping Liu, Lian Duan, and Jian-Xun Wang. Bayesian conditional diffusion models for versatile spatiotemporal turbulence generation. *Computer Methods in Applied Mechanics and Engineering*, 427:117023, 2024.
- [41] Tobias Sebastian Finn, Charlotte Durand, Alban Farchi, Marc Bocquet, Pierre Rampal, and Alberto Carrassi. Generative diffusion for regional surrogate models from sea-ice simulations. *Journal of Advances in Modeling Earth Systems*, 16(10):e2024MS004395, 2024.
- [42] Gefan Yang and Stefan Sommer. A denoising diffusion model for fluid field prediction. *arXiv preprint arXiv:2301.11661*, 2023.
- [43] Roberto Molinaro, Samuel Lanthaler, Bogdan Raonić, Tobias Rohner, Victor Armegioiu, Stephan Simonis, Dana Grund, Yannick Ramic, Zhong Yi Wan, Fei Sha, et al. Generative ai for fast and accurate statistical computation of fluids. *arXiv preprint arXiv:2409.18359*, 2024.
- [44] Alvaro Sanchez-Gonzalez, Jonathan Godwin, Tobias Pfaff, Rex Ying, Jure Leskovec, and Peter Battaglia. Learning to simulate complex physics with graph networks. In *International conference on machine learning*, pages 8459–8468. PMLR, 2020.
- [45] Tobias Pfaff, Meire Fortunato, Alvaro Sanchez-Gonzalez, and Peter Battaglia. Learning mesh-based simulation with graph networks. In *International conference on learning representations*, 2020.

- [46] Johannes Brandstetter, Daniel Worrall, and Max Welling. Message passing neural pde solvers. *arXiv preprint arXiv:2202.03376*, 2022.
- [47] Mario Lino, Stathi Fotiadis, Anil A Bharath, and Chris Cantwell. Towards fast simulation of environmental fluid mechanics with multi-scale graph neural networks. *arXiv preprint arXiv:2205.02637*, 2022.
- [48] Filipe De Avila Belbute-Peres, Thomas Economou, and Zico Kolter. Combining differentiable pde solvers and graph neural networks for fluid flow prediction. In *international conference on machine learning*, pages 2402–2411. PMLR, 2020.
- [49] Hojin Kim, Varun Shankar, Venkatasubramanian Viswanathan, and Romit Maulik. Generalizable data-driven turbulence closure modeling on unstructured grids with differentiable physics. *arXiv e-prints*, pages arXiv–2307, 2023.
- [50] Alvaro Sanchez-Gonzalez. Graphcast: Learning skillful medium-range global weather forecasting. *European Geosciences Union General Assembly 2024 (EGU24)*, page 11381, 2024.
- [51] Gang Liu, Jiaxin Xu, Tengfei Luo, and Meng Jiang. Graph diffusion transformers for multi-conditional molecular generation. *Advances in Neural Information Processing Systems*, 37:8065–8092, 2024.
- [52] Yuyang Wang, Zijie Li, and Amir Barati Farimani. Graph neural networks for molecules. In *Machine learning in molecular sciences*, pages 21–66. Springer, 2023.
- [53] Seonghwan Kim, Jeheon Woo, and Woo Youn Kim. Diffusion-based generative ai for exploring transition states from 2d molecular graphs. *Nature Communications*, 15(1):341, 2024.
- [54] Kai Yi, Bingxin Zhou, Yiqing Shen, Pietro Liò, and Yuguang Wang. Graph denoising diffusion for inverse protein folding. *Advances in Neural Information Processing Systems*, 36:10238–10257, 2023.
- [55] Ilan Price, Alvaro Sanchez-Gonzalez, Ferran Alet, Tom R Andersson, Andrew El-Kadi, Dominic Masters, Timo Ewalds, Jacklynn Stott, Shakir Mohamed, Peter Battaglia, et al. Gencast: Diffusion-based ensemble forecasting for medium-range weather. *arXiv preprint arXiv:2312.15796*, 2023.
- [56] Haomin Wen, Youfang Lin, Yutong Xia, Huaiyu Wan, Qingsong Wen, Roger Zimmermann, and Yuxuan Liang. Diffstg: Probabilistic spatio-temporal graph forecasting with denoising diffusion models. In *Proceedings of the 31st ACM international conference on advances in geographic information systems*, pages 1–12, 2023.
- [57] Giuseppe Alessio D’Inverno, Kylian Ajavon, and Simone Brugiapaglia. Surrogate models for diffusion on graphs via sparse polynomials. *arXiv preprint arXiv:2502.06595*, 2025.
- [58] Mario Lino, Tobias Pfaff, and Nils Thuerey. Learning distributions of complex fluid simulations with diffusion graph networks. *arXiv preprint arXiv:2504.02843*, 2025.
- [59] Mario Lino Valencia, Nils Thuerey, and Tobias Pfaff. Se (3)-equivariant diffusion graph nets: Synthesizing flow fields by denoising invariant latents on graphs. In *ICML 2024 AI for Science Workshop*, 2024.
- [60] Geir Evensen. The ensemble kalman filter: Theoretical formulation and practical implementation. *Ocean dynamics*, 53(4):343–367, 2003.
- [61] Marc Bocquet, Julien Brajard, Alberto Carrassi, and Laurent Bertino. Data assimilation as a learning tool to infer ordinary differential equation representations of dynamical models. *Nonlinear Processes in Geophysics*, 26(3): 143–162, 2019.
- [62] Caterina Buizza, César Quilodrán Casas, Philip Nadler, Julian Mack, Stefano Marrone, Zainab Titus, Clémence Le Cornec, Evelyn Heylen, Tolga Dur, Luis Baca Ruiz, et al. Data learning: Integrating data assimilation and machine learning. *Journal of Computational Science*, 58:101525, 2022.
- [63] Elizabeth G Ryan, Christopher C Drovandi, James M McGree, and Anthony N Pettitt. A review of modern computational algorithms for bayesian optimal design. *International Statistical Review*, 84(1):128–154, 2016.
- [64] Burr Settles. Active learning literature survey. 2009.
- [65] Yarin Gal, Riashat Islam, and Zoubin Ghahramani. Deep bayesian active learning with image data. In *International conference on machine learning*, pages 1183–1192. PMLR, 2017.
- [66] Ali Siahkoobi, Gabrio Rizzuti, and Felix J Herrmann. Deep bayesian inference for seismic imaging with tasks. *Geophysics*, 87(5):S281–S302, 2022.
- [67] Antoine Blanchard and Themistoklis Sapsis. Bayesian optimization with output-weighted optimal sampling. *Journal of Computational Physics*, 425:109901, 2021.
- [68] Vivek Oommen, Siavash Khodakarami, Aniruddha Bora, Zhicheng Wang, and George Em Karniadakis. Learning turbulent flows with generative models: Super-resolution, forecasting, and sparse flow reconstruction. *arXiv preprint arXiv:2509.08752*, 2025.

- [69] Meet Hemant Parikh, Yaqin Chen, and Jian-Xun Wang. D-flow sgld: Source-space posterior sampling for scientific inverse problems with flow matching. *arXiv preprint arXiv:2602.21469*, 2026.
- [70] Dibyajyoti Chakraborty, Haiwen Guan, Jason Stock, Troy Arcomano, Guido Cervone, and Romit Maulik. Multimodal atmospheric super-resolution with deep generative models. *Machine Learning: Earth*, 2025.
- [71] Jiahe Huang, Guandao Yang, Zichen Wang, and Jeong Joon Park. Diffusionpde: Generative pde-solving under partial observation. *Advances in Neural Information Processing Systems*, 37:130291–130323, 2024.
- [72] Jan-Hendrik Bastek, WaiChing Sun, and Dennis M Kochmann. Physics-informed diffusion models. *arXiv preprint arXiv:2403.14404*, 2024.
- [73] Hongkai Zheng, Wenda Chu, Bingliang Zhang, Zihui Wu, Austin Wang, Berthy T Feng, Caifeng Zou, Yu Sun, Nikola Kovachki, Zachary E Ross, et al. Inversebench: Benchmarking plug-and-play diffusion priors for inverse problems in physical sciences. *arXiv preprint arXiv:2503.11043*, 2025.
- [74] Christian Jacobsen, Yilin Zhuang, and Karthik Duraisamy. Cocogen: Physically consistent and conditioned score-based generative models for forward and inverse problems. *SIAM Journal on Scientific Computing*, 47(2): C399–C425, 2025.
- [75] Changyuan Zhao, Guangyuan Liu, Bin Xiang, Dusit Niyato, Benoit Delinchant, Hongyang Du, and Dong In Kim. Generative ai enabled robust sensor placement in cyber-physical power systems: a graph diffusion approach. *arXiv preprint arXiv:2501.06756*, 2025.
- [76] Yeong Woo Son and Jong Min Lee. A diffusion-attention-based algorithm for optimal spatio-temporal sensor placement in distributed parameter systems. *Computers & Chemical Engineering*, 200:109163, 2025.
- [77] Abhijeet Vishwasrao, Sai Bharath Chandra Gutha, Andres Cremades, Klas Wijk, Aakash Patil, Catherine Gorle, Beverley J McKeon, Hossein Azizpour, and Ricardo Vinuesa. Diff-sport: Diffusion-based sensor placement optimization and reconstruction of turbulent flows in urban environments. *arXiv preprint arXiv:2506.00214*, 2025.
- [78] Chen Wang, Victoria Huang, Gang Chen, Hui Ma, Bryce Chen, and Jochen Schmidt. Learning to optimise climate sensor placement using a transformer. *arXiv preprint arXiv:2310.12387*, 2023.
- [79] Dibyajyoti Chakraborty, Seung Whan Chung, Troy Arcomano, and Romit Maulik. Divide and conquer: Learning chaotic dynamical systems with multistep penalty neural ordinary differential equations. *Computer Methods in Applied Mechanics and Engineering*, 432:117442, 2024.
- [80] Gustavo Deco, Christian Schittkopf, and Bernd Schürmann. Determining the information flow of dynamical systems from continuous probability distributions. *Physical review letters*, 78(12):2345, 1997.
- [81] Xiaokai Nie and Daniel Coca. Reconstruction of one-dimensional chaotic maps from sequences of probability density functions. *Nonlinear Dynamics*, 80(3):1373–1390, 2015.
- [82] Jonah Botvinick-Greenhouse, Maria Oprea, Romit Maulik, and Yunan Yang. Measure-theoretic time-delay embedding. *Journal of Statistical Physics*, 192(12):171, 2025.
- [83] Dibyajyoti Chakraborty, Shivam Barwey, Hong Zhang, and Romit Maulik. A note on the error analysis of data-driven closure models for large eddy simulations of turbulence. *arXiv preprint arXiv:2405.17612*, 2024.
- [84] J-P Eckmann and David Ruelle. Ergodic theory of chaos and strange attractors. *Reviews of modern physics*, 57(3): 617, 1985.
- [85] Christophe Abraham, Gérard Biau, and Benoit Cadre. On lyapunov exponent and sensitivity. *Journal of mathematical analysis and applications*, 290(2):395–404, 2004.
- [86] M Kay Steven et al. Fundamentals of statistical signal processing. *PTR Prentice-Hall, Englewood Cliffs, NJ*, 10 (151045):148, 1993.
- [87] Emily Clark, Steven L Brunton, and J Nathan Kutz. Multi-fidelity sensor selection: Greedy algorithms to place cheap and expensive sensors with cost constraints. *IEEE Sensors Journal*, 21(1):600–611, 2020.
- [88] Niharika Karnik, Mohammad G Abdo, Carlos E Estrada-Perez, Jun Soo Yoo, Joshua J Cogliati, Richard S Skifton, Patrick Calderoni, Steven L Brunton, and Krithika Manohar. Constrained optimization of sensor placement for nuclear digital twins. *IEEE Sensors Journal*, 24(9):15501–15516, 2024.
- [89] Kimberly Stachenfeld, Drummond B Fielding, Dmitrii Kochkov, Miles Cranmer, Tobias Pfaff, Jonathan Godwin, Can Cui, Shirley Ho, Peter Battaglia, and Alvaro Sanchez-Gonzalez. Learned coarse models for efficient turbulence simulation. *arXiv preprint arXiv:2112.15275*, 2021.
- [90] Yair Schiff, Zhong Yi Wan, Jeffrey B Parker, Stephan Hoyer, Volodymyr Kuleshov, Fei Sha, and Leonardo Zepeda-Núñez. Dyslim: Dynamics stable learning by invariant measure for chaotic systems. *arXiv preprint arXiv:2402.04467*, 2024.

- [91] Thomas Frerix, Dmitrii Kochkov, Jamie Smith, Daniel Cremers, Michael Brenner, and Stephan Hoyer. Variational data assimilation with a learned inverse observation operator. In *International Conference on Machine Learning*, pages 3449–3458. PMLR, 2021.
- [92] Varun Shankar, Vedant Puri, Ramesh Balakrishnan, Romit Maulik, and Venkatasubramanian Viswanathan. Differentiable physics-enabled closure modeling for burgers’ turbulence. *Machine Learning: Science and Technology*, 4(1):015017, 2023.
- [93] Dmitrii Kochkov, Jamie A. Smith, Ayya Alieva, Qing Wang, Michael P. Brenner, and Stephan Hoyer. Machine learning–accelerated computational fluid dynamics. *Proceedings of the National Academy of Sciences*, 118(21), 2021. ISSN 0027-8424. doi: 10.1073/pnas.2101784118. URL <https://www.pnas.org/content/118/21/e2101784118>.
- [94] Dmitrii Kochkov, Jamie A Smith, Ayya Alieva, Qing Wang, Michael P Brenner, and Stephan Hoyer. Machine learning–accelerated computational fluid dynamics. *Proceedings of the National Academy of Sciences*, 118(21): e2101784118, 2021.
- [95] Bassem F Armaly, F Durst, JCF Pereira, and B Schönung. Experimental and theoretical investigation of backward-facing step flow. *Journal of fluid Mechanics*, 127:473–496, 1983.
- [96] J. SMAGORINSKY. GENERAL CIRCULATION EXPERIMENTS WITH THE PRIMITIVE EQUATIONS. *Monthly Weather Review*, 91(3):99–164, March 1963. doi: 10.1175/1520-0493(1963)091<0099:gcewtp>2.3.co;2. URL [https://doi.org/10.1175/1520-0493\(1963\)091<0099:gcewtp>2.3.co;2](https://doi.org/10.1175/1520-0493(1963)091<0099:gcewtp>2.3.co;2).
- [97] Igor A Baratta, Joseph P Dean, Jørgen S Dokken, Michal Habera, Jack HALE, Chris N Richardson, Marie E Rognes, Matthew W Scroggs, Nathan Sime, and Garth N Wells. Dolfinx: the next generation fenics problem solving environment. 2023.
- [98] Shivam Barwey, Pinaki Pal, Saumil Patel, Riccardo Balin, Bethany Lusch, Venkatram Vishwanath, Romit Maulik, and Ramesh Balakrishnan. Mesh-based super-resolution of fluid flows with multiscale graph neural networks. *Computer Methods in Applied Mechanics and Engineering*, 443:118072, 2025.

## A Training and Sampling Hyperparameters

### A.1 Homogeneous Isotropic Turbulence

We use a DDPM++-style U-Net (SongUNet) [30] with positional timestep embedding, standard encoder/decoder, and circular padding for periodic boundaries. The model is trained to denoise with the EDM objective. Noise levels  $\sigma$  are sampled log-normally with  $\log \sigma \sim \mathcal{N}(P_{\text{mean}}, P_{\text{std}}^2)$ . For the multi-step trained model we use the same model and train with  $n_{\text{steps}} = 4$  future steps and a short curriculum (single step for the first 1000 kimg, then full  $n_{\text{steps}}$ ). Gradient checkpointing is also enabled to fit larger batches. The error prediction network used for the predictive sensor placement is a small encoder-decoder U-Net with base 64 channels, multipliers [1, 2, 4, 8], two conv blocks per resolution, BatchNorm, ReLU, and dropout 0.1, and outputs a non-negative error map. For sampling, we use the EDM sampler (Heun-style, second-order) with a log-linear  $\sigma$  schedule in  $\rho$ -space. For unconditional generation we run the sampler from Gaussian noise; for conditioned (posterior) generation, we use the same sampler with an added likelihood score term, using the required sensor placement (Ref. Chakraborty et al. [70]). Other hyperparameters are mentioned in Table 1. These hyperparameters have been tuned empirically using a smaller subset of data and for a shorter training time.

### B Backwards Facing Step

We use the graph neural network diffusion model with EDM preconditioning mentioned in Section 2.4. The multi-step training setup uses the same model and trains over  $K = 4$  rollout steps. We did not notice any effect of curriculum training here, as we set up the model to predict the difference between the current timestep (condition) and the forecast. Apart from these, we use similar training and sampling setup as for the homogeneous isotropic turbulence case. We reuse the same spatial U-Net structure (voxel pooling, same lengthscales) but with `hidden_channels = 128`, no time embedding, and TransformerConv blocks (4 heads, dropout 0.1) for the error prediction model; the diffusion backbone is frozen and the prediction model is trained at  $\sigma = 80$  (pure noise) to match diffusion forecast error magnitude. The other hyperparameters are mentioned in Table 1.

Table 1: Consolidated training and sampling hyperparameters for Homogeneous Isotropic Turbulence (HIT) and Backwards-Facing Step (BFS) experiments.

Hyperparameter	Homogeneous Isotropic Turbulence		Backwards-Facing Step (BFS)	
	Single	Multi	Single	Multi
<i>Model Architecture</i>				
Backbone type	SongUNet		Custom GNN in Section 2.4	
Base / Hidden channels	32		256	
Channel multipliers	[1, 2, 4, 8, 16]		-	
Attention resolutions	[64, 64], [32, 32], [16, 16]		All (4 heads)	
Encoder/Decoder layers	Standard		3 / [2, 2, 2] blocks	
Padding / Voxel scales	Circular (periodic)		[0.015, 0.03, 0.06]	
<i>Compute Details</i>				
GPU resource	8 NVIDIA A100		12 Intel Data Center Max 1550 Series	
Training Time(hrs)	48		36	
<i>Optimizer &amp; Trainer</i>				
Optimizer	AdamW	AdamW	AdamW	AdamW
Learning rate	$5 \times 10^{-4}$	$5 \times 10^{-4}$	$5 \times 10^{-4}$	$5 \times 10^{-4}$
Unroll steps ( $n_{steps}$ )	1	4	1	4
Total training (king)	20,000	20,000	10,000	10,000
LR ramp-up (king)	2,000	500	1,000	1,000
Curriculum (king)	-	1,000	-	-
<i>EDM Preconditioning &amp; Sampling</i>				
$\sigma_{min} / \sigma_{max}$	0.005 / 80	0.005 / 80	0.002 / 80	0.002 / 80
$P_{\mu} / P_{\sigma}$	-1 / 1.5	-1 / 1.5	-0.2/2.2	-0.2/2.2
ODE Steps	50	50	30	30
$\rho$ schedule	7	7	7	7
$S_{churn} / S_{noise}$	80 / 1.003	80 / 1.003	80 / 1.003	80 / 1.003
$S_{min} / S_{max}$	0.01 / 50	0.01 / 50	0.01 / 50	0.01 / 50